

Old Dogs, New Tricks: Re-examining Photographic Spectra of Plaskett’s Star

T. J. DAVIDGE¹

¹*Dominion Astrophysical Observatory,
Herzberg Astronomy & Astrophysics Research Center,
National Research Council of Canada, 5071 West Saanich Road,
Victoria, BC Canada V9E 2E7
tim.davidge@nrc.ca; tdavidge1450@gmail.com*

ABSTRACT

Photographic spectra of Plaskett’s Star (PS; HR2420, HD47129, V640 Mon) that were recorded at the Dominion Astrophysical Observatory (DAO) have been digitized with a flatbed scanner. Many of the spectra were recorded during campaigns in 1922 and 1937, and sample wavelengths between 0.39 and 0.50 μ m. Spectra of poor quality are identified. Mean spectra near orbital phases 0.25 and 0.75 match many characteristics of synthetic spectra, although H γ and He I λ 4388 are exceptions. Evidence is presented that H γ was affected by transient activity in 1937, but not in 1922. Emission lines of N III and He II move with wavelength in a manner that is consistent with them tracking the motion of the secondary, indicating that an ‘f’ spectral type designation should be assigned to the secondary. The location of the peak that is associated with the secondary in cross-correlation functions changes with time near phase 0.75, although the mean amplitude of the radial velocity curve of the secondary did not change between the two campaigns. There is also an offset in velocities of the primary measured from H γ and He I λ 4472 near phase 0.25. The velocity curves of the components suggest a mass ratio that is larger than previous estimates, although uncertainties associated with the spectroscopic features attributed to the secondary, coupled with the wavelength resolution of the spectra, complicate efforts to determine robust masses. We conclude that the peculiarities in the radial velocity curves of the components have thus been in place for over a thousand orbital cycles.

1. INTRODUCTION

In a pioneering paper that is one of the first discussions of a non-solar stellar spectrum in the published literature, [Draper \(1877\)](#) examined absorption lines in a spectrum of Vega that was recorded on a photographic plate. While other highly innovative means of capturing astronomical spectra were implemented over the next century (e.g. [Oke 1969](#); [Robinson & Wampler 1972](#)), photographic plates remained the most commonly used detectors for spectroscopic observations until the widespread use of CCDs in the 1980s. As a result, photographic spectra are often the only means of examining the spectroscopic properties of stars prior to circa 1980.

There are a number of well-known shortcomings inherent to photographic plates, including low quantum efficiency, non-linearity, the inherent fragility of glass, and the vulnerability of the emulsion to damage. Still, the non-digital nature of photographic material is arguably the most fundamental impediment to their use. To date, the digitization of plates has largely been done with specialized machines that operate in carefully controlled environments. Limited access to these devices, combined with an inherently inefficient scanning process, can frustrate and complicate the digitization of photographic observations.

The situation has changed with the availability of compact, high-quality flatbed scanners. While earlier generations of scanners failed to capture the full information content of photographic spectra (e.g. [Simcoe 2009](#); [Davidge 2024](#)), this has changed with the current generation of top-of-the-line models. A pragmatic demonstration of this is that stellar spectra digitized with an Epson 12000-XL scanner compare favorably with those recorded with CCDs (e.g. Figures 10 and 11 of [Davidge 2024](#)). The use of flatbed scanners greatly simplifies the digitization process – with a comparatively modest financial investment, it is now possible to capture efficiently the information content of photographic spectra in an office environment.

The Dominion Astrophysical Observatory (DAO) hosts a large collection of photographic spectra that were recorded on its telescopes over much of the past century. The largest number of plates were recorded with the original

Cassegrain spectrograph on the 1.8 meter telescope (Plaskett 1918), starting in 1918, while the Coudé spectrograph on the 1.2 meter telescope (Richardson 1968) has been in use since 1962. Many stars have been observed numerous times with these facilities, resulting in datasets that can be used to study long-term behaviour over timescales of many decades.

In the current paper we examine digitized spectra of the binary system Plaskett’s Star (V640 Mon, HR2420, HD47129; hereafter PS). PS was targeted early in the operational life of the 1.8 meter telescope as part of a survey of emission-line O stars, and it was soon found to be a double line spectroscopic binary (SB2). A subsequent ~ 1 year observing campaign revealed velocity variations with a ~ 14 day period that were indicative of massive components (Plaskett 1922). At the time, PS was the most massive system known.

While more massive systems have since been identified (e.g. Melnick 34 and HD38282, both in the LMC), PS remains one of the most massive binary systems to be detected in the Galaxy, and our knowledge of the basic properties of its components, including spectral types, luminosities, effective temperatures, surface gravities, and rotation velocities continues to evolve. Isolating spectroscopic signatures of the primary (defined here to be the brighter star at optical wavelengths) and the secondary (the fainter star) are key to determining their properties. Unfortunately, the spectrum of PS contains a mix of absorption and emission lines that appear to originate from a number of sources, and the complex nature of the composite spectrum confounded early efforts to isolate the spectrum of the secondary.

Emission associated with the Balmer and He lines was first noted by Plaskett (1922) and Struve (1948). The latter concluded that many of the weaker lines in the PS spectrum are non-stellar, and suggested that emission from a gas stream may contribute significantly to the light. Struve et al. (1958) noted that the weaker lines appear not to follow the orbital motion of the secondary, and discussed evidence for a shell, arguing that He I lines that are blue-shifted by ~ 700 km/sec originate from such a structure. Hutchings & Cowley (1976) found that the emission associated with He II $\lambda 4686$ may not be related kinematically to either star, while N emission at 4485 and 4503Å may move with the primary.

Given that the components appear to be massive early-type stars then winds likely play a significant role in shaping the intrasystem and circumsystem environments. The ratio of the x-ray to bolometric flux from PS is similar to that found in O star binaries that likely contain colliding winds (Linder et al. 2006). Some of the lines in the UV that are attributed to the secondary have P Cygni profiles, indicating an extended circumstellar region (Bagnuolo et al. 1992). The properties of the intercomponent region may largely be defined by the wind from the secondary, which may dominate over that of the primary (Wiggs & Gies 1992).

Variability in spectroscopic characteristics further complicates understanding the components of PS. Struve et al. (1958) found that the spectrum changes with time, with ‘large and erratic fluctuations’ in the weaker lines that are attributed to the secondary. Linder et al. (2006) detect variations in the strengths of N and Fe lines in the X-ray regime, signaling that variability occurs over a range of wavelengths, species, and excitation conditions. There are also subtle line strength variations that may not be tied directly to the orbital properties of the system. The wings of H α emission change on timescales of ~ 2 days (Wiggs & Gies 1992), suggesting that the intracomponent medium is structured. Palate & Rauw (2014) identified two sub-orbital frequencies in spectroscopic properties, and conclude that these might originate from the secondary, the primary, or both. Non-radial pulsations, tidal interactions, and magnetic confinement of winds were considered as possible mechanisms for this variability, although Palate & Rauw conclude that none of these explanations is problem-free.

There are indications that the stars in PS have interacted, and if there has been large-scale mass transfer then this could complicate efforts to isolate the spectroscopic signatures of the components. For example, one expected consequence of mass transfer is a rapidly rotating secondary due to a gain in angular momentum from the primary, and evidence for such rapid rotation is seen (e.g. Struve 1948; Bagnuolo et al. 1992; Bagnuolo & Barry 1996; Grunhut et al. 2022), including a flattening of the secondary in the orbital plane (Linder et al. 2008). Not only does rotation smear lines and make them harder to detect, it may also complicate efforts to assign a luminosity class due to gravity darkening (e.g. Linder et al. 2008). A disk may also form that veils the host star.

There are chemical signatures indicating that the primary has evolved off of the ZAMS. Models of massive systems discussed by Sen et al. (2022) find that N is enhanced in a donor after the onset of Roche lobe overflow (RLOF), and that the He content increases as mass is lost. In contrast, N and He enhancement may be modest in the accretor due to rotational mixing. Bagnuolo & Barry (1996) and Linder et al. (2006, 2008) find that the primary has non-solar abundance ratios, being deficient in C and O, while N is enhanced, which is consistent with CNO processing.

Linder et al. (2008) also find that the secondary is overabundant in He and deficient in N. They note that the chemical abundances of both stars are consistent with post-RLOF evolution, with the rapid rotation of the secondary affecting its N abundance.

If there have been interactions between the components then their properties should differ from those of isolated stars. The large-scale transfer of mass due to RLOF is expected to leave a primary that is substantially more luminous than would otherwise be expected for its present-day mass (e.g. Sen et al. 2022), exacerbating the difference in luminosity that might have once existed between the two stars. Bagnuolo et al. (1992), Bagnuolo & Barry (1996) and Linder et al. (2008) conclude that the ratio of fluxes in the blue and visual is ~ 0.5 . Despite this difference, the stars appear to have similar spectral types (e.g. Hutchings & Cowley 1976). Bagnuolo et al. (1992) decouple the spectra of the components to reveal spectral types O7.5I and O6I, while Linder et al. (2008) assign spectral types O8 III/I and O7.5III.

Another complicating factor is that some of the motions detected in the spectra may not be associated with the orbital motions of the components, and this is compounded by the challenges isolating the spectrum of the secondary. Given the difficulties detecting the spectrum of the secondary, Plaskett (1922) used the radial velocities of the primary to obtain the orbital elements of the system, with the radial velocities of the secondary used only to obtain the amplitude of the velocity variations of that star. He found a mass ratio (i.e. the mass of the secondary divided by that of the primary) ~ 0.8 with a non-zero orbital eccentricity.

Subsequent studies confirmed that the radial velocities attributed to the components may not faithfully track their orbital motions. Based on 73 spectra that covered two orbital cycles, Struve (1948) noted that the radial velocity curve of the primary changes between cycles, and that the orbital eccentricity obtained from the velocity curve varies with time. The radial velocity curve of the secondary was offset from that predicted by Plaskett’s solution by ~ 100 km/sec.

The problematic nature of the radial velocity curve of the secondary is not restricted to older datasets, where there might be difficulties isolating the centroids of weak, broad features. Stickland (1997) examined cross-correlation functions (CCFs) based on UV spectra at different orbital phases, and concluded that the motion attributed to the secondary ‘makes no sense’, as the position of the peak in the CCF that is associated with the secondary does not define the same rest velocity as the primary. In addition, Linder et al. (2008) found that while the velocities measured for the primary over a wide range of wavelengths are consistent with each other, the agreement among velocities measured for the secondary is not as good.

Grunhut et al. (2022) conclude that the rapidly rotating secondary is a magnetic star, and found that the Stokes V profiles are consistent with radial velocity variations that are substantially smaller than those found previously. More recent spectropolarimetric observations discussed by Stacey et al. (2024) suggest that the radial velocity variation of the secondary may be even smaller than the 30 km/sec variation found by Grunhut et al. (2022). The velocity of the secondary notwithstanding, it must have a mass of at least $12.6M_{\odot}$. Stickland (1987) combined velocities measured for the primary in the UV with all other published velocities at blue wavelengths to obtain a ‘grand solution’, and a mass function of $12.6 M_{\odot}$ was found for a circular orbit. While the inclination of the system is uncertain, Stickland estimated that the secondary has a mass of at least $60 M_{\odot}$. Bagnuolo et al. (1992) subsequently combined additional velocity measurements with those considered by Stickland (1987), and found a mass ratio 1.18 ± 0.12 . This is in contrast to most previous work, as it suggests that the secondary is more massive than the primary, as would be expected if there has been mass transfer. Based largely on orbital information defined by the primary, Linder et al. (2008) estimate ‘best’ masses of 55 and $57 M_{\odot}$ assuming an inclination of 71 degrees.

PS is a photometric variable, and the light curve provides additional clues into the nature of the system. When phased according to the orbital period, the light curve is asymmetric with an amplitude of a few hundredths of a magnitude (Mahy et al. 2011; Grunhut et al. 2022). This modest amplitude is evidence that the structural properties of PS have changed considerably since the termination of mass transfer, as the lack of ellipsoidal variations of even moderate amplitude suggests that the components are not distorted by close proximity to their critical Roche surfaces. Still, interactions between the components due to stellar winds are not precluded, and the photometric variations may be due to activity on the primary that could be the product of shock-heated material. Mahy et al. (2011) found other periodicities in the light curve that are attributed to non-radial pulsations. The photometry produces tight light curves when phased to a period that is much shorter than that attributed to orbit motions, with a range in the periods deduced from different datasets (Grunhut et al. 2022).

The stellar content in the vicinity of PS contains additional clues into its age and evolution. Astrometric information obtained from the GAIA DR3 (Gaia Collaboration 2016; ?) indicates that it is associated with Mon OB2 and the young cluster NGC 2244 (Davidge 2022), which has an age ~ 5.5 Myr (Bonatto & Bica 2009). However, this is not an ironclad age estimate as star formation in a cluster environment may proceed over many millions of years (e.g. Bik et al. 2019). Indeed, while Davidge (2022) finds an entourage of stars that are associated with PS, none appear to be pre-main sequence objects (Linder et al. 2008), suggesting that PS is not in a star-forming environment at present.

In this paper we discuss photographic spectra of PS recorded with DAO telescopes that have been digitized with a flatbed scanner. The intent is to explore the information that can be extracted from the spectra, and demonstrate that the plates are more than curious historical artifacts from a bygone era. As the spectra sample a five decade timeframe, and thus cover more than one thousand orbital cycles, they provide a unique perspective on the spectroscopic properties of PS throughout much of the past century, prior to the advent of modern detectors. Many of the spectra were recorded during campaigns that were conducted over a single observing season, and in some cases this allows for a comparison of properties between consecutive orbital cycles.

2. PLATE SELECTION AND CHARACTERISTICS

All plates of PS in the DAO collection were digitized, and a list of these is provided in Tables 1 (1.8 meter observations) and 2 (1.2 meter observations). The plate number, date of observation, orbital phase and other information are listed. The orbital phase was computed from the ephemeris in Table 2 of Linder et al. (2008), where phase 0 is primary inferior conjunction. To the best of our knowledge the 1.8 meter spectra recorded in the 1930s and later have not been discussed in the published literature.

Table 1. Plate Information: 1.8 meter

Plate #	Date (YYYY MM DD)	HJD – 2400000	Orbital Phase ^b	Notes ^a
6858	1921 12 01	23025.967	0.361	
6906	1921 12 16	23040.949	0.402	
6953	1921 12 29	23053.838	0.297	
6960	1922 01 01	23056.874	0.508	
7006	1922 01 12	23067.849	0.270	short camera
7095	1922 01 29	23084.802	0.448	short camera
7138	1922 02 18	23104.753	0.834	
7142	1922 02 19	23105.660	0.897	
7161	1922 02 20	23106.693	0.969	
7168	1922 02 20	23106.802	0.976	short camera
7193	1922 02 23	23109.733	0.180	
7209	1922 02 24	23110.632	0.242	
7213	1922 02 24	23110.736	0.249	
7217	1922 02 25	23111.675	0.315	
7232	1922 02 26	23112.619	0.380	
7234	1922 02 26	23112.785	0.392	
7243	1922 02 27	23113.647	0.452	
7264	1922 02 28	23114.769	0.530	
7280	1922 03 07	23121.680	0.010	
7282	1922 03 10	23124.689	0.219	

Table 1 continued on next page

Table 1 (*continued*)

Plate #	Date (YYYY MM DD)	HJD – 2400000	Orbital Phase ^b	Notes ^a
7284	1922 03 12	23126.667	0.357	
7289	1922 03 16	23130.640	0.632	
7294	1922 03 16	23130.780	0.642	short camera
7301	1922 03 18	23132.635	0.771	
7302	1922 03 18	23132.808	0.783	
7304	1922 03 19	23133.633	0.840	
7330	1922 03 22	23136.697	0.053	
7335	1922 03 23	23137.667	0.120	
7385	1922 03 31	23145.661	0.675	
7392	1922 04 03	23148.670	0.884	
7403	1922 04 04	23149.664	0.953	
7412	1922 04 05	23150.658	0.022	
8334	1922 11 11	23370.027	0.260	damaged
21768	1933 11 05	27382.047	0.945	
21794	1933 12 03	27409.917	0.881	alignment?
23677	1935 02 03	27836.799	0.498	alignment?
26180	1936 10 08	28449.999	0.128	
26211	1936 10 15	28457.019	0.616	
26236	1936 10 17	28459.062	0.758	
26282	1936 10 25	28467.033	0.311	alignment?
26304	1936 11 01	28474.032	0.797	bad
26329	1936 11 07	28480.082	0.218	bad
26367	1936 11 21	28494.051	0.188	
26376	1936 11 24	28497.026	0.395	bad
26399	1936 11 26	28499.004	0.532	bad
26400	1936 11 26	28499.067	0.536	alignment?
26506	1937 01 02	28535.838	0.091	
26517	1937 01 06	28539.837	0.368	
26525	1937 01 07	28540.759	0.432	
26529	1937 01 08	28541.765	0.502	
26541	1937 01 11	28544.881	0.719	alignment?
26568	1937 01 19	28552.854	0.272	
26594	1937 01 31	28564.802	0.102	
26626	1937 02 14	28578.796	0.075	
26640	1937 02 25	28589.790	0.838	alignment?
26646	1937 02 28	28592.650	0.037	
26649	1937 03 03	28595.736	0.251	
26654	1937 03 06	28598.674	0.455	
26665	1937 03 15	28607.657	0.079	
26666	1937 03 15	28607.690	0.082	

Table 1 continued on next page

Table 1 (*continued*)

Plate #	Date (YYYY MM DD)	HJD – 2400000	Orbital Phase ^b	Notes ^a
26681	1937 03 16	28608.656	0.149	
26694	1937 03 18	28610.730	0.293	
26712	1937 03 29	28621.657	0.052	alignment?
26718	1937 04 06	28629.687	0.610	
26726	1937 04 07	28630.661	0.677	
27391	1937 10 22	28829.056	0.458	
27678	1938 03 07	28964.737	0.883	red cut-off
28624	1938 10 06	29178.027	0.699	
28992	1938 12 25	29257.906	0.247	
29083	1939 02 23	29317.714	0.402	
29090	1939 02 24	29318.835	0.480	
A22101	1939 02 28	29322.704	0.748	
A22112	1939 03 04	29326.639	0.022	alignment?
A22113	1939 03 04	29326.681	0.025	
A22114	1939 03 04	29326.737	0.028	alignment?
A22124	1939 03 09	29331.684	0.372	
A22125	1939 03 09	29331.738	0.376	
29122	1940 03 23	29711.992	0.789	
29174	1940 04 10	29729.673	0.017	
29772	1940 11 18	29952.000	0.461	
31966	1942 11 25	30688.948	0.651	Wavelength calibration?
44460	1953 01 06	34383.740	0.300	
47265+6	1954 11 07	35054.004	0.859	Short camera, two spectra

^aMost spectra were recorded with the medium focus 29Å/mm camera, while a small number were recorded with the short focus 55Å/mm camera. The spectra with an ‘alignment’ entry in the last column have blurred lines and an uneven response with wavelength. It is suspected that these problems were due to unstable optical alignment in the spectrograph (see text, and Figure 5).

^bFrom orbital elements in Table 2 of [Linder et al. \(2008\)](#).

Some of the plates have a poor signal to noise ratio (S/N) and/or cosmetic flaws, such as scratches on the emulsion, fingerprints, and staining that occurred during the development of the plate. Plates with cosmetic flaws are indicated in the fifth column, and these are most common among the 1.2 meter spectra recorded in 1974. Some of the spectra recorded for the 1937 campaign are affected by what appear to be optical alignment issues in the spectrograph, and these are discussed in more detail in Section 4. Whereas the centers of deep lines can be measured in those plates, their utility for the examination of line depth and strength is limited.

The 1.8 meter spectra were recorded through a slit with a prism as the dispersing element. The wavelength coverage extends from 0.39 to 0.50 μ m, with the short wavelength cut-off largely defined by the throughput of the prism. This wavelength interval was targeted extensively in the early days of the DAO as it samples numerous features that are useful for velocity measurements ([Plaskett 1918](#)). As these are slit spectra then the wavelength resolution and line profiles are susceptible to variations in the seeing. While seeing variations are to be expected at any ground-based observing site, they tend to be common in the DAO spectra of PS given that it has a meridian airmass of ~ 1.4 at DAO.

Table 2. Plate Information: 1.2 meter

Plate #	Date (YYYY MM DD)	HJD – 2400000	Orbital Phase ^b	Notes ^a
4345	1969 03 07	40287.701	0.404	
4419	1969 03 24	40304.671	0.583	
5146	1969 10 23	40518.006	0.402	
5386	1970 02 11	40628.757	0.095	
6576	1971 02 07	40989.713	0.168	
7352	1972 04 19	41426.699	0.522	
7379	1972 05 05	41442.699	0.633	
8804	1974 02 05	42083.885	0.172	
8820	1974 02 20	42098.685	0.200	
8825	1974 02 22	42100.844	0.350	poor cosmetics
8907	1974 03 21	42127.684	0.214	poor cosmetics
8908	1974 03 21	42127.718	0.216	No arc
9329	1974 09 21	42312.012	0.018	poor cosmetics
9421	1974 10 09	42329.927	0.262	poor cosmetics
9467	1974 10 19	42339.979	0.961	Long camera; weak lines
9480	1974 10 29	42349.928	0.652	poor cosmetics
9481	1974 10 29	42349.960	0.654	poor cosmetics
9545	1975 01 10	42422.938	0.723	
9566	1975 01 29	42441.693	0.026	
9584	1975 02 25	42468.658	0.899	
9592	1975 02 26	42469.674	0.970	poor cosmetics
9600	1975 03 06	42477.700	0.527	low S/N
9607	1975 03 10	42481.679	0.803	
9618	1975 03 11	42482.692	0.874	
9641	1975 03 27	42498.681	0.985	

^aMost of the spectra were recorded with the 32121 grating mosaic (10.1Å /mm). Plates identified as having poor cosmetics are affected by non-uniformities in development and/or fingerprints.

^bFrom orbital elements in Table 2 of [Linder et al. \(2008\)](#).

Most of the 1.8 meter spectra were recorded with the medium focus 28Å/mm camera, although some were recorded with the short focus 55Å/mm camera. The latter have a smaller physical size on the plate when compared with the former. However, the S/N and wavelength resolution of the digitized spectra from both cameras are similar, indicating that the characteristics of the camera optics are not limiting factors for defining the intrinsic wavelength resolution of these spectra.

The 1.8 meter spectra from the 1920s and 1930s were recorded on Eastman 40 plates that were probably not hypersensitized. [Plaskett \(1921\)](#) discusses early negative experiences with hypersensitization at the DAO, leading us to suspect that the spectra recorded in 1922 – 1923 were not hypersensitized. In section 4 it is shown that most of the plates recorded with the 1.8 meter at later dates have responses that are very similar to the spectra recorded in the 1920s, suggesting that they also were not hypersensitized or, if our suspicions about hypersensitization are incorrect, they were hypersensitized with the same procedure used in 1922.

The 1.2 meter spectra were recorded with an image slicer, which suppresses the potential for guiding errors while also improving throughput. The majority of these spectra were recorded with the 32121 grating mosaic (10.1Å

/mm), although some spectra were also recorded with the 3262 (9.0Å /mm) and 3282 (6.5Å /mm) gratings. The wavelength coverage of the 1.2 meter spectra typically extends from 0.35 μ m to 0.55 μ m, and we place emphasis on the 0.39 to 0.50 μ m interval for compatibility with the 1.8 meter spectra.

The 1.2 meter spectra were recorded on Kodak type II or III plates with wavelength responses tuned to sample near-ultraviolet to visible wavelengths. Mees (1933, 1935) discusses the various Kodak plate types used for spectroscopic applications. The 1.2 meter plates were hypersensitized with either forming gas or Hg vapor.

Arc spectra bracket the PS spectrum on the vast majority of plates, and these are used for wavelength calibration. All of the 1.2 meter spectra as well as the 1.8 meter spectra recorded in the 1930s and at later dates have a calibration region to assess the photometric response. However, the signal tends to be saturated throughout much of this calibration region, and there is scattered light from saturated areas. In addition, unless the exposure time for the calibration signal is comparable to that of the stellar spectrum then reciprocity failure may also produce differences in response between the stellar spectra and calibration signal (e.g. Mees 1931). Given that the utility of this calibration information is unclear, then the intensity measurements of the spectra presented throughout this paper are based on the density of activated grains in the photographic emulsion. A differential approach for comparing spectra based on an assessment of response characteristics is thus adopted (Section 4).

3. SCANNING & PROCESSING

The plates were digitized with an Epson 12000XL scanner. Davidge (2024) demonstrated that the optical quality of this device is sufficient to recover the information content in spectra that were recorded with the 1.8 meter Cassegrain spectrograph. A scanning density of 2400 dpi was used, which corresponds to a spatial resolution of $\sim 10\mu$ m. This is comparable to, or smaller than, the grain size of most photographic emulsions.

The digitized spectra were processed according to the procedures described by Davidge (2024). All processing was done with tasks in IRAF (Tody 1986, 1993). The processing included background subtraction using measurements near the plate edges to suppress signal from scattered light and plate fogging.

Unlike the spectra of Vega that were examined by Davidge (2024), the spectral resolution of the PS data typically does not change along the slit, and this is likely due to the longer exposure times for the PS spectra. Still, there are a modest number of exceptions that are likely due to seeing, and the manner in which the slit is illuminated by the wings of the point spread function. Experimentation found that signal that is within 20% of the peak value of the mean illumination profile constructed by averaging the light distribution along the slit tended to have a stable spectral resolution. Therefore, signal within 20% of the mean peak signal was extracted from each plate for further processing. In addition to stability in spectral resolution, this extraction criterion also restricts the final spectra to those parts of the light profile that have the highest S/N, while also reducing the effect of scattered light from the arcs that closely bracket the 1.8 meter spectra. In contrast, there is a distinct gap between the arc and stellar spectra on the 1.2 meter plates. Residual signatures of bright arc lines are not evident in any of the extracted spectra.

The signal in individual columns of each digitized spectrum was summed, and a wavelength calibration that was based on a linear interpolation of the arcs that bracket each spectrum was applied. The wavelength calibration was then placed in the heliocentric frame. The wavelength calibrated spectra were normalized to a pseudo-continuum that was based on a polynomial fit to each spectrum. Recursive clipping was used to suppress absorption and emission lines when fitting the continuum.

Some 1.8 meter spectra recorded in the 1930s appear to be affected by optical alignment problems that we suspect are due to flexure and mechanical issues in the spectrograph. Evidence for mis-alignment comes in the form of satellites and sub-structures in arc lines, as well as periodic undulations in the continuum that have an amplitude of up to $\sim 10\%$ and are likely due to scattered light. An effort was made to remove the variations in the continuum by fitting high-order polynomials, although this had mixed success and affected the wings of broad lines, such as H γ . These spectra are discussed further in Section 4.2.

4. CHARACTERISTICS OF THE SPECTRA

4.1. General Properties

There are two sets of 1.8 meter spectra and one set of 1.2 meter spectra that were recorded over the course of a single observing season. For the remainder of the paper we refer to spectra recorded between December 1 1921 and March 5 1922 as belonging to the 1922 campaign, while those obtained between October 8 1936 and March 7 1937 belong to the 1937 campaign. Spectra recorded with the 1.2 meter between September 21 1974 and March 27 1975

belong to the 1975 campaign. The two 1.8 meter campaigns provide insights into the properties of PS over a 15 year baseline. The 1.2 meter spectra extend the time coverage by another four decades, although many of those spectra are of poor quality (Table 2).

The average properties of spectra in each campaign have been examined to assess similarities and differences. Spectra that were recorded for each campaign were aligned on the centers of $H\gamma$ and He I $\lambda 4471$, and the results were combined by taking the median signal at each wavelength. Spectra identified in Table 1 as having a poor S/N were not included. Given that (1) the primary star is the dominant contributor to the system light near 4400\AA , and (2) the alignment was done using features that are prominent in its spectrum, then the combined spectra are expected to be largely representative of the primary. Still, the high rotational velocity of the secondary means that there will likely be residual signatures from that star in each combined spectrum.

4.1.1. 1.8 Meter Spectra

The median spectra constructed from the 1922 and 1937 campaigns are compared in Figure 1. The difference between these, in the sense 1922 – 1937, is shown at the bottom of the figure. At first glance, a comparison of the campaign spectra reveals few surprises. As expected for O stars, the deepest absorption features are those of H and He. In addition to absorption lines, there are also a number of emission features. Emission is present in the wings of $H\beta$, but is not obvious in the higher order Balmer lines. N III emission at 4630 and 4634\AA and He II emission at 4686\AA are also present. The N emission is a signature of the ‘f’ sub-class for O stars, while He II $\lambda 4686$ in emission is indicative of a supergiant luminosity class (e.g. Martins 2018).

It is shown below that N III emission moves with orbital phase in the same sense as the secondary. The N III lines in Figure 1 are thus blurry residuals, and so do not represent these features as they would appear in individual spectra. The central absorption feature in the He II emission profile also moves in a manner that is consistent with it belonging to the secondary, and this is contrary to what was found by Hutchings & Cowley (1976). The broad DIB band near 4430\AA , which is one of the deepest interstellar features in the blue - red wavelength region (e.g. Herbig 1975), is also apparent.

The overall throughput of both sets of 1.8 meter spectra is highest between 0.42 and $0.48\mu\text{m}$ and, with the exception of $H\gamma$ (see below), there is good agreement between the median campaign spectra at these wavelengths, with a dispersion in the differenced spectrum between 0.44 and $0.48\mu\text{m}$ of $\sim \pm 1\%$. The agreement between the median spectra at these wavelengths suggests that the plates recorded for the two campaigns tend to have similar response characteristics, at least among features that (1) have strengths that are within $\sim 10\%$ of the continuum, and (2) are the result of combining many plates to suppress environmental variations, such as differences in wavelength resolution due to seeing variations. The comparison in Figure 1 thus opens the possibility of making differential comparisons between the two sets of 1.8 meter spectra in the $0.42 - 0.48\mu\text{m}$ wavelength region, at least when considering differences on the order of 1% or higher. This has broad implications for plates in the DAO collection as it suggests that spectra of other stars recorded at the DAO between 1921 and 1938 should thus have similar response characteristics.

$H\gamma$ appears to be a special case, as it is the one feature between 0.44 and $0.48\mu\text{m}$ that changes with time. While the depths of $H\gamma$ in the spectra differ at the $\sim 5\%$ level, a similar difference is not seen for He I $\lambda 4471$. We suspect that the difference in the depths of $H\gamma$ between the two spectra in Figure 1 is not an artifact of the response of the photographic plates, as $H\gamma$ and He I $\lambda 4471$ are close together in wavelength, and the He line has an intrinsic depth that is not greatly different from that of $H\gamma$. These features should then sample similar parts of the characteristic curve of each plate. While these are slit spectra, the difference in $H\gamma$ depth is not due to guiding errors and seeing variations, as these would affect the characteristics of all lines in similar proportion, which is not the case in Figure 1. The behaviour of $H\gamma$ is examined further in Section 4.2.

The differences between the campaign spectra grow in size outside of the wavelength interval where the throughput is highest. $H\delta$ and He I $\lambda 4026$ are stronger in the 1922 spectrum, differing from the depth in the 1937 campaign spectrum by between 5 and 10%. As for $H\beta$, it is weaker in the 1922 spectrum, and in Section 4.2 evidence is presented for variations in the shape of this line, likely due to emission.

4.1.2. 1.2 meter Spectra

A subset of the 1975 campaign spectra were also median-combined, and the result is shown in Figure 2. Many of the PS plates recorded with the 1.2 meter have cosmetic flaws that are largely due to problems with the development process and plate handling (e.g. fingerprints). The median spectrum shown in Figure 2 was constructed from the five

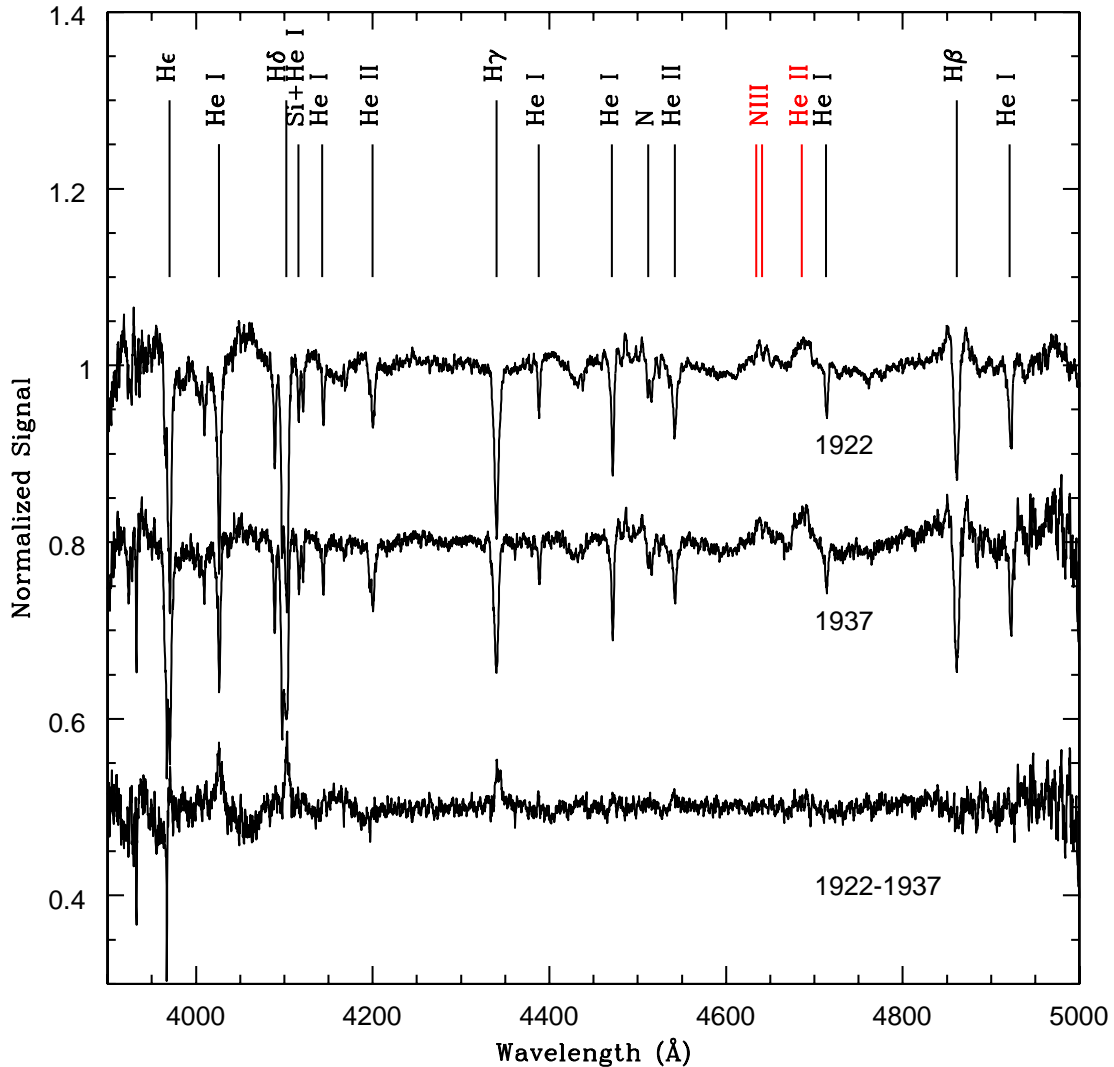


Figure 1. Median 1.8 meter spectra of PS, constructed by taking the pixel-by-pixel median of individual campaign spectra after aligning to the rest wavelengths of $H\gamma$ and $He\ I\ \lambda 4471$. As with all other figures in this paper, the vertical axis is a measure of the density of activated grains in the emulsion, and has not been corrected for departures from linearity. Given the relative brightnesses of the component stars, the median spectra are largely representative of the primary, as features associated with the secondary are suppressed or blurred. Still, some features that are associated with the secondary remain (see text). The S/N diminishes near the blue and red edges of the spectra due to the lower throughput at these wavelengths. The difference between the two spectra is shown at the bottom. The depths of the Balmer lines and $He\ I\ \lambda 4026$ differ at the $\sim 5\%$ level. However, between 4400 and 4800Å, where the throughput is highest, the variance in the difference is $\sim \pm 1\%$. It is argued in the text that the difference in the depth of $H\gamma$ is not due to plate characteristics. (Note: The data used to construct this figure will be made available online in the published version of this paper).

spectra that do not have cosmetic issues, which are plates 9545, 9566, 9584, 9607, and 9641. The spectrum that results if more spectra are combined has slightly different absorption line depths.

A comparison of the 1975 and 1922 campaign spectra in Figure 2 indicates that the spectral resolution of the 1.2 meter spectra, as gauged from the widths of absorption lines, is not greatly different from that of the 1.8 meter spectra. The largest difference in resolution is apparent in the character of $He\ II\ \lambda 4686$ emission, which appears as two well-separated peaks in the 1.2 meter data. The general similarity of the 1.2 meter and 1.8 meter campaign spectra is noteworthy given that the 1.2 meter plates were recorded more than three decades after the 1937 campaign, and so use

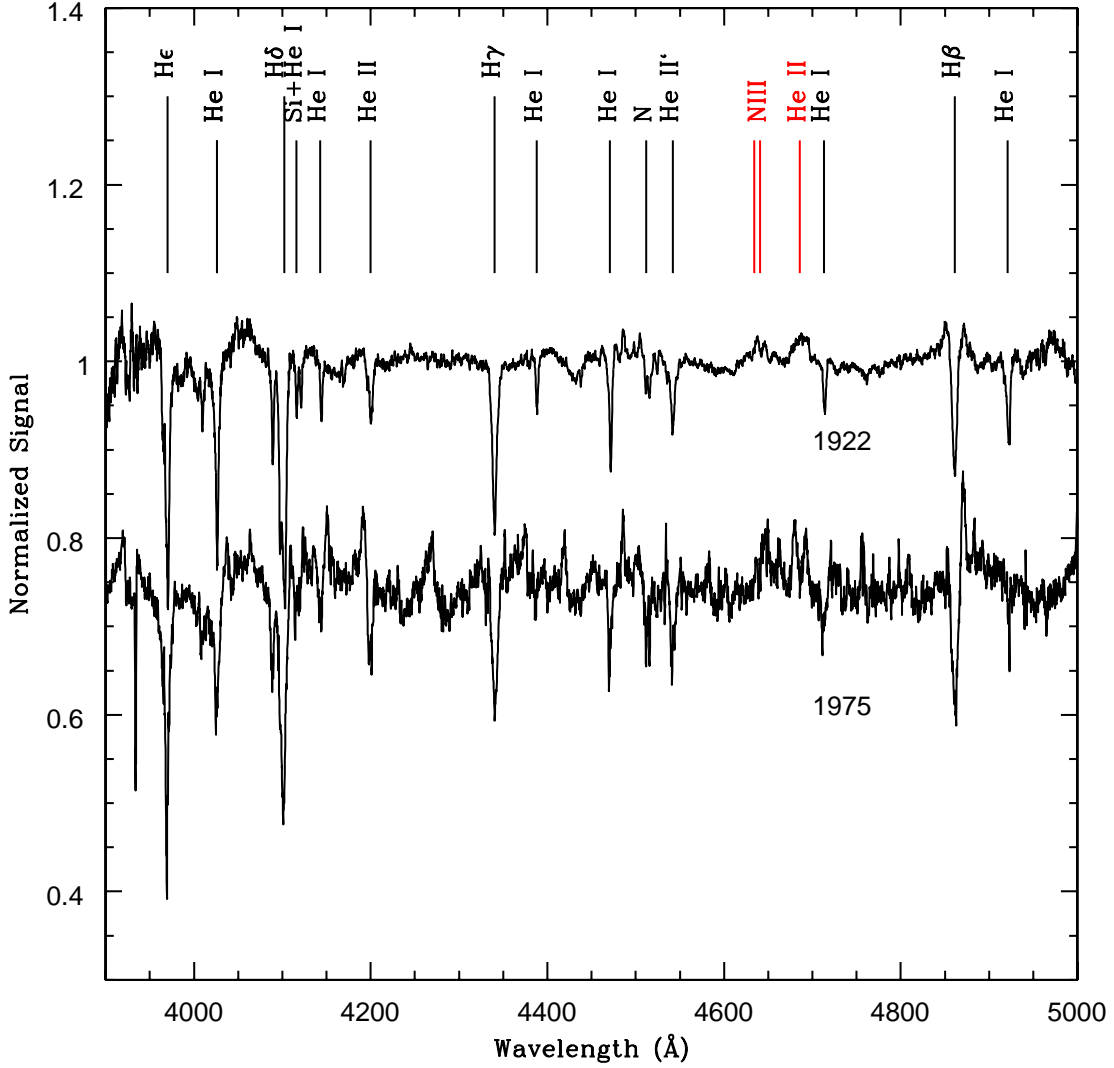


Figure 2. Composite 1975 campaign spectrum of PS, constructed from the five spectra recorded during that campaign that do not have major cosmetic defects. As with the spectra in Figure 1, individual spectra were shifted to align $H\gamma$ and $He\ I\ \lambda 4471$ with their rest wavelengths before taking the median at each pixel. The median 1922 campaign spectrum from Figure 1 is also shown. The differences between the 1975 and 1922 campaign spectra are similar to those between the 1937 and 1922 spectra in Figure 1. Still, while there is not a large difference in the widths of absorption lines, there is a noticeable difference in the properties of $He\ II\ \lambda 4686$ emission, which appears as two distinct components in the 1.2 meter spectrum. (Note: The data used to construct this figure will be made available online in the published version of this paper).

different emulsions and hypersensitization techniques. In addition, the 1.2 meter spectra were recorded with an image slicer, and so the spectral resolution should be less susceptible to seeing variations than the 1.8 meter slit spectra.

4.2. Consistency

While Figures 1 and 2 demonstrate that there is an overall consistency between DAO spectra recorded in the 1920s and 1930s when their average characteristics are considered, there are significant plate-to-plate variations in the characteristics of absorption features, and these are examined in this section. The intrinsic depths of features in the spectrum of an interacting binary change with orbital phase, due to variations in the observed brightness of each star as well as the motions of lines with wavelength during an orbital cycle. To suppress these, we compare spectra in

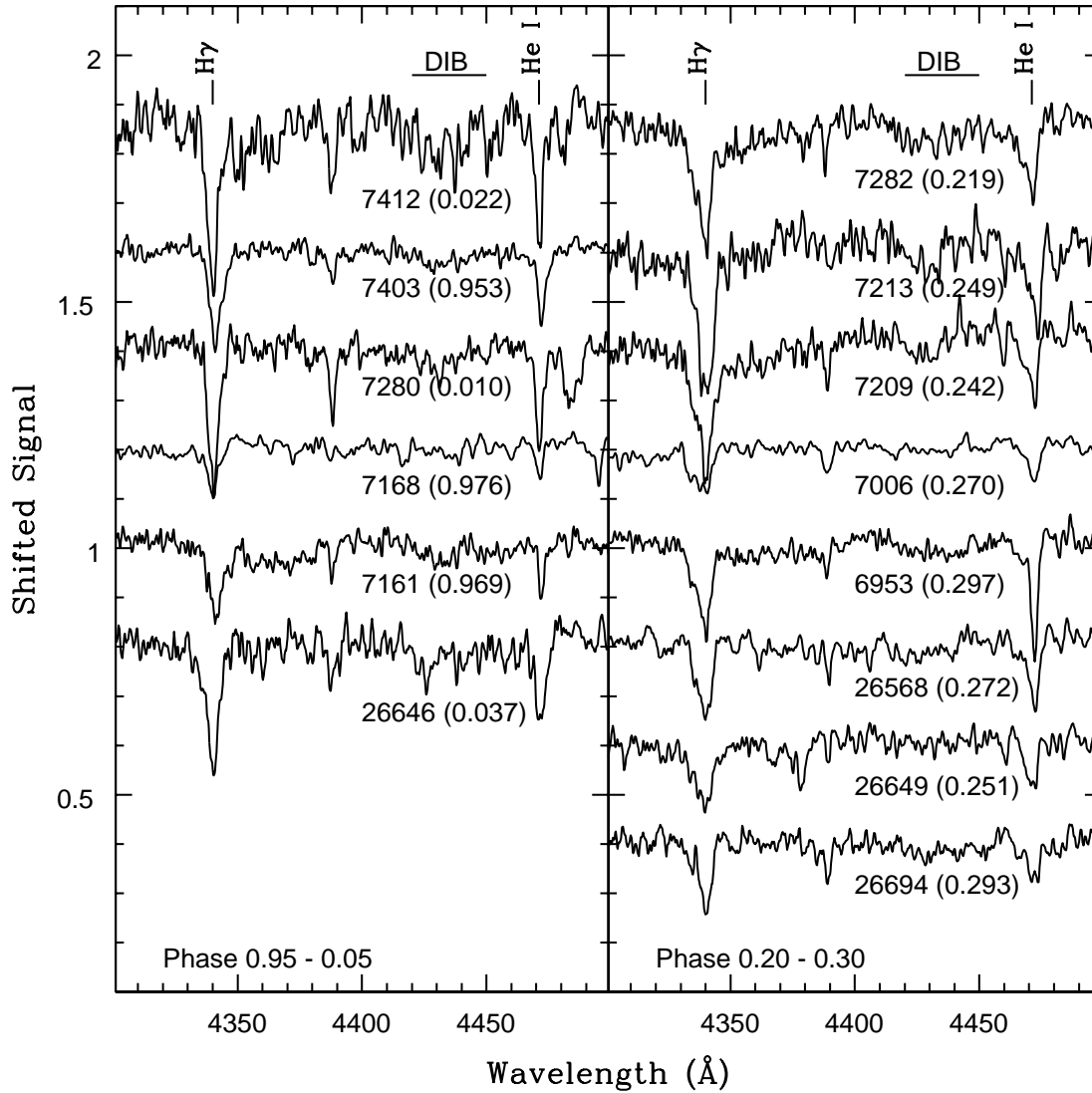


Figure 3. Selected spectra in the wavelength interval 4300 to 4500Å that were recorded during the 1920s and 1930s. Orbital phases are in brackets next to the plate numbers. Spectrum-to-spectrum variations in the absolute and relative depths of H γ and He I λ 4471 are seen. The depths of H γ and He I λ 4471 vary in sync in most cases, as expected if the range in line characteristics is not a result of intrinsic spectroscopic variations, but is instead due to observational effects, such as seeing variations. Still, the depths of H γ and He I λ 4471 in spectra 6953 and 26568 are comparable, hinting at an intrinsic origin for the variation in some features. With the exception of spectrum 26646, the sharpest and deepest features are seen in the 1922 campaign spectra, and this is consistent with the relative depths of features in the median spectra in Figure 1.

narrow orbital phase intervals. The 1.2 meter spectra are not included in these comparisons given the limited number of cosmetically 'good' spectra.

The depths of prominent lines in the 1922 and 1937 campaigns in the orbital phase intervals 0.95 - 0.05 and 0.2 - 0.3 are compared in Figures 3 (H γ and He I λ 4471) and 4 (H β). H γ and He I λ 4471 are separated by only 130Å, and are at wavelengths where the overall system throughput is highest. Barring intrinsic variations in line strengths in one or both of the components then H γ and He I λ 4471 should vary in lockstep.

The lines in Figures 3 and 4 have similar behaviour, in the sense that the spectra with the deepest lines in Figure 3 also have the deepest H β line in Figure 4. There is an expectation that the relative depths of H γ and He I λ 4471 should vary in sync. However, while He I λ 4471 is slightly shallower than H γ in most cases, two exceptions

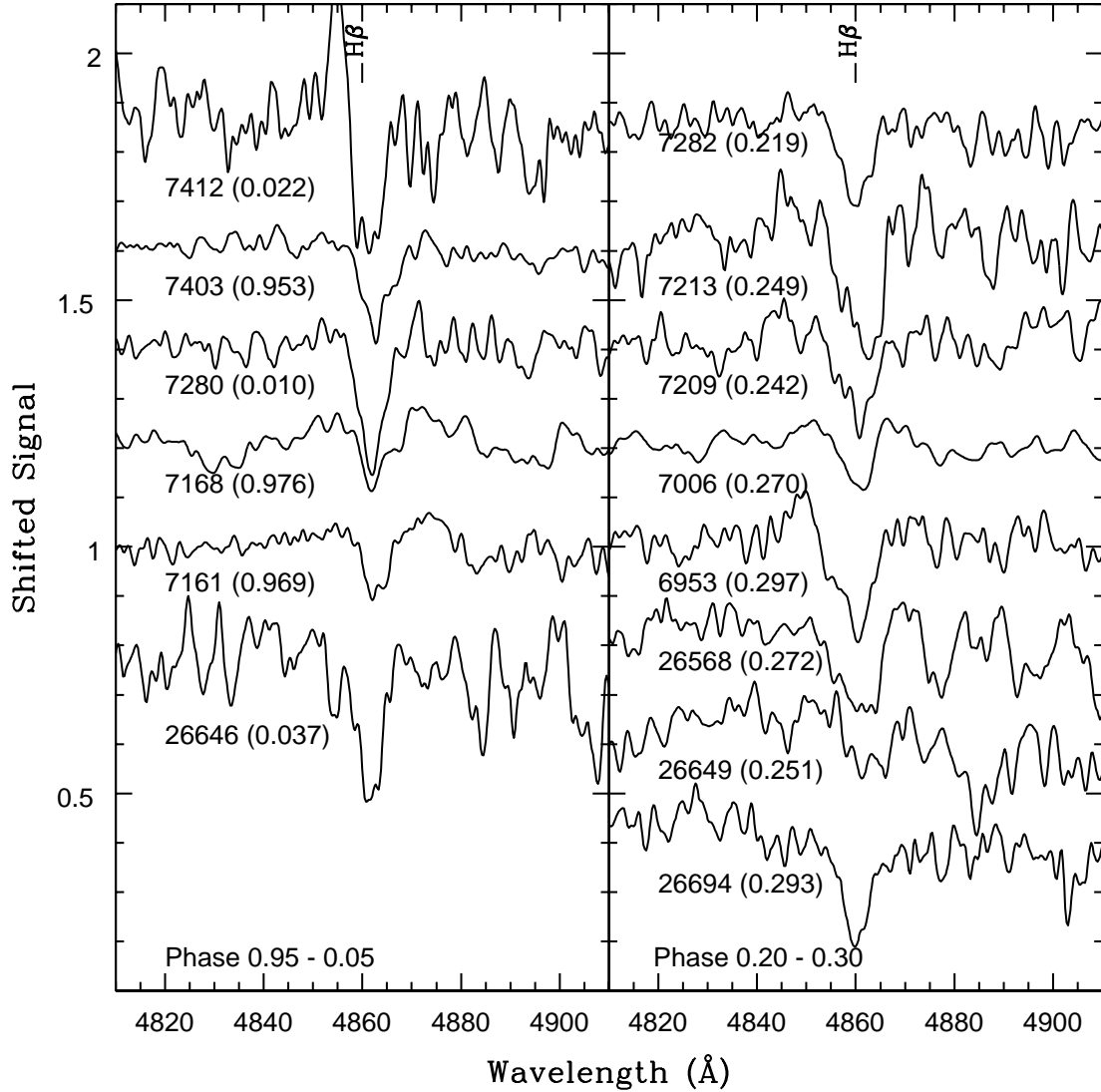


Figure 4. Same as Figure 4, but showing $H\beta$. $H\beta$ is on the shoulder of the response curve where the overall throughput is markedly lower than near $H\gamma$ and He I $\lambda 4471$, and so the spectra are noisier than in Figure 3. There is a clear dispersion in the depths and shape of $H\beta$, in the sense that the character of the line core varies with time, changing from a pointed to a flat or double-pointed morphology.

are the spectra extracted from plates 6953 and 26568, where $H\gamma$ and He I $\lambda 4471$ have similar depths. This is another indication that the depth of $H\gamma$ may be subject to variations that are intrinsic to the spectrum of the primary, rather than observing conditions.

The comparisons in Figure 4 are compromised somewhat by the S/N, although there is a clear dispersion in the depth of $H\beta$. The shape of $H\beta$ changes with time, in the sense that there is a pointed line core at some epochs, and a flat core at others. Variations of this nature are seen in the spectra of evolved O stars. For example, the O supergiant HD192639 has a spectral type that is similar to that of the components in PS. $H\beta$ in the spectrum of this star has a variable morphology like that seen in Figure 4 (Rauw & Vreux 1998).

If large scale spectroscopic variations over the timescales of a few hours are absent in PS then spectra that are recorded on the same night are an important means of examining the consistency of the photographic spectra, and may provide insights into the nature of any plate-to-plate differences. Three spectra of PS were recorded with the 1.8

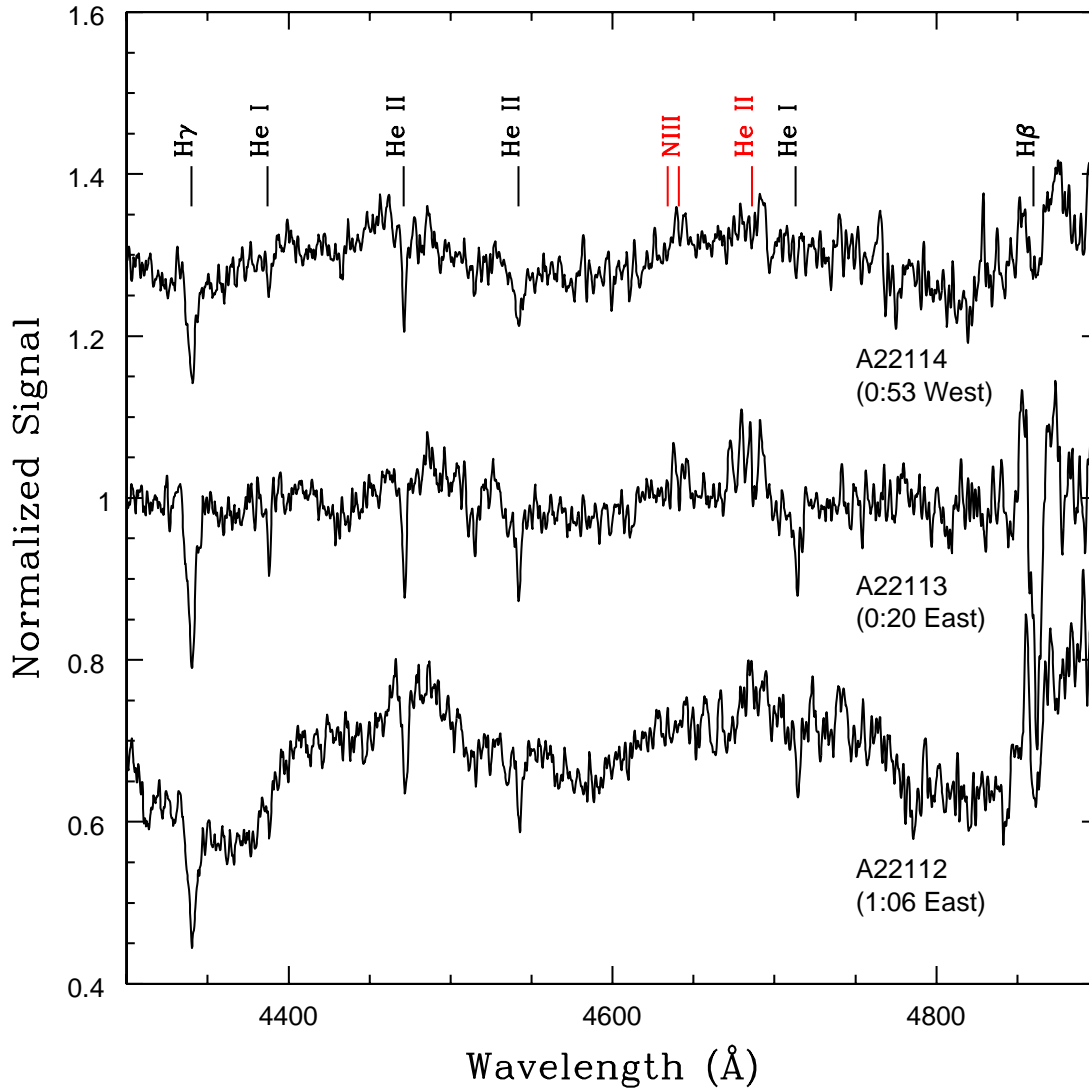


Figure 5. Spectra recorded with the 1.8 meter telescope on the night of March 4, 1939. The hour angle at the start of the exposures is shown in brackets; spectrum A22113 was recorded as PS transited the meridian. The spectra have been normalized to a high-order polynomial that was fit to the pseudo-continuum in an attempt to remove large-scale variations in the system response, while not affecting the depths of absorption lines. However, the highest order polynomial that could safely be applied to the A22112 and A22114 spectra left residual variations in the pseudo-continuum. These variations are periodic and synced in phase, suggesting a common origin. There is a tendency for the absorption lines to be broader and shallower in A22112 than in the other spectra, while the A22113 spectrum has a comparatively flat pseudo-continuum coupled with the sharpest and deepest lines. In contrast to plate A22113, the arc lines on the A22112 and A22114 plates have conspicuous satellites, suggesting that the variations in the pseudo-continuum are due to optical alignment issues, possibly arising from flexure in the spectrograph due to the orientation of the telescope ('flopture').

meter on the night of March 4 1939, and these are plates A22112, A22113, and A22114. The spectra extracted from these plates are compared in Figure 5.

The hour angle at the start of each exposure is shown in brackets under the plate number in Figure 5. The A22112 spectrum was recorded one hour to the east of the meridian and has an uneven continuum. Similar, but lower amplitude variations, are seen in the A22114 spectrum, which was recorded one hour to the west of the meridian. The uneven nature of the continuum is a feature that is shared with other spectra recorded during the 1930s, and these are indicated with the 'alignment?' entry in the right hand column of Table 2. The A22113 spectrum has the sharpest lines

and the flattest continuum in Figure 5, and this spectrum was recorded while PS was crossing the meridian. While absorption lines are visible in all three spectra, signalling that they might be useful for velocity measurements, there are differences in the depths and widths of lines that appear to be correlated with the amplitude of the continuum fluctuations, and these frustrate studies of line profiles.

The spectrum-to-spectrum differences in Figures 3, 4, and 5 are likely due to a number of factors. The spectra with poor S/N are easiest to explain. The sky transparency tends to be poor during the winter in Victoria, with variations in cloud cover occurring over short timescales. Exposures that were started in what were initially acceptable conditions might then be truncated prematurely, with only a fraction of the intended signal recorded.

The 1.8 meter spectra were recorded through a slit, and so differences in line depth due to seeing and/or guiding errors might be expected. PS culminates on the sky at DAO near an airmass of 1.4. Given the roughly one hour exposure time required to obtain a photographic spectrum of PS, coupled with the relatively high airmass and awkward positioning of the telescope while observing PS and the need for manual guiding at the time these data were recorded, then the spectra are likely susceptible to seeing variations and – possibly – guiding errors. Both of these will affect the wavelength resolution of slit spectra, such as are apparent in Figures 3 and 4. Additional evidence that observational factors may dominate the dispersion in line properties was presented earlier in the paper, where the median campaign spectra, in which variations due to observing conditions are suppressed, were found to agree for most (but not all) lines.

The continuum variations in the A22112 and A22114 spectra are periodic and synchronized in wavelength. This is indicative of a common origin, and suggests that they are not due to plate flaws, issues with the development process, or seeing fluctuations. Rather, we suspect that the continuum variations have an origin that is related to the spectrograph. The arc emission lines on these plates have satellites that are suggestive of an optical alignment issue, and the number of plates in Table 1 that are flagged with alignment issues in Table 1 suggest that this was not a rare occurrence in the 1930s. Problems with optical alignment may occur if there is flexure in the spectrograph as the telescope tracks an object at high airmass. Flexure would be less of a problem when the target is close to the meridian. This is consistent with the behaviour of the spectra in Figure 5.

4.3. Variations with Orbital Phase

Given the spectrum-to-spectrum differences discussed in the previous section, whenever possible we consider the means of spectra to examine changes in line properties with orbital phase. The averaging of spectra suppresses environmental factors, and so should provide a more homogeneous dataset when making differential comparisons. Systematic factors, such as the non-linear response of the photographic plate, are not suppressed.

Mean spectra in the orbital phase ranges 0.15 – 0.35 and 0.65 – 0.85 are shown in Figures 6 (1922 campaign), 7 (1937 campaign), and 8 (1975 campaign). These phases sample the points in the orbit where the wavelength separation between the spectra of the components is greatest, and so should then provide the most reliable insights into their spectral types and relative luminosities. Three wavelength regions centered on $H\gamma$, $H\beta$ and the N III emission lines are shown in Figures 6 and 7. The wavelength interval that covers $H\beta$ is not shown in Figure 8 as the S/N of the 1.2 meter spectra at these wavelengths is poor. The motion of lines due to the orbital motions of the components are evident in all three figures, as are changes in line shape. The latter are due in large part to the orbital motion of the secondary, the spectrum of which moves with respect to that of the primary and forms a notch in the line profiles.

The relative depths of $H\gamma$ and He I $\lambda 4471$ is a measure of spectral type. The locations of the notch that is due to the secondary in the line profiles indicates that He I/ $H\gamma$ is smaller in the secondary than in the primary, suggesting that the secondary has a later spectral type than the primary. Moreover, the $H\gamma$ and He I profiles near phases 0.25 and 0.75 do not mirror each other, in that the notch in the line profile that is attributed to the secondary near phase 0.25 is not seen at the same depth as that near phase 0.75. This is demonstrated in Figure 9, where the profiles of $H\gamma$ and He I $\lambda 4471$ from Figures 6, 7, and 8 are overplotted. The mean spectrum from the 1937 campaign spectrum for phases 0.65 – 0.85 has been scaled by a factor of 1.5 in this figure to match the depth of $H\gamma$ between phases 0.15 and 0.35.

The green lines in Figure 9 mark the location of the notch from the secondary in the $H\gamma$ profile. The location of this notch in the 1922 spectrum is three quarters of the way down the $H\gamma$ line between phases 0.15 and 0.35, but is only half way down the profile at phases 0.65 – 0.85. This asymmetry indicates that the systemic velocity estimated from the radial velocity curve of the secondary differs from that of the primary. This is consistent with the earlier

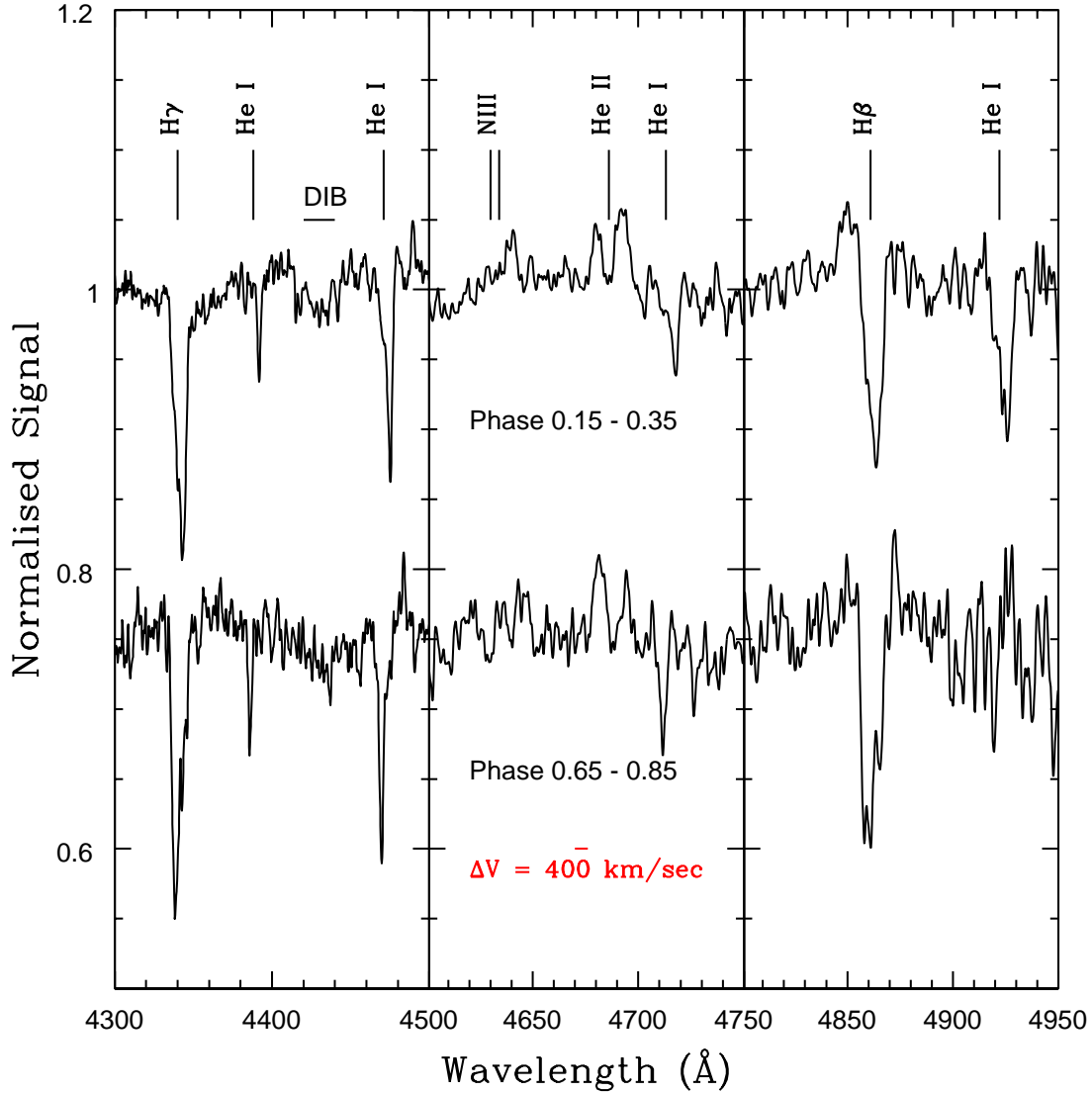


Figure 6. Mean 1922 campaign spectra in the orbital phase intervals 0.15 - 0.35 and 0.65 - 0.85. The horizontal red line in the middle panel shows the maximum shift in wavelength due to the motion of the primary (i.e. $\sim 6\text{\AA}$). Shifts in the mean wavelengths of H and He absorption lines as well as changes in their profiles due to the motion of the secondary are seen. While N III emission is weak between phases 0.15 and 0.35, it is more pronounced near phase 0.75. The character of He II $\lambda 4686$ and the emission in the shoulders of $H\beta$ both change with orbital phase. The central absorption component of He II $\lambda 4686$ and the $H\beta$ emission follows the motion of the secondary.

analyses by [Plaskett \(1922\)](#) and [Stickland \(1997\)](#), both of whom found that the components have different mean space velocities.

The disagreement between systemic velocities does not occur at all epochs. The notch due to the secondary in the 1937 $H\gamma$ profile occurs at roughly the same depth near phases 0.25 and 0.75 indicating that the systemic velocities obtained from the radial velocities of the primary and secondary from those data should agree. Differences in the kinematic properties of the 1922 and 1937 campaign spectra are examined further in Section 6, where the CCFs of individual spectra near phases 0.25 and 0.75 are compared, as well as in the Appendix, where radial velocities obtained from individual spectra are discussed.

What could cause the systemic velocities of the 1922 and 1937 spectra to differ? If there is an optically thick absorbing medium with bulk motions that differ from the orbital motions of the stars, then variations in the radial

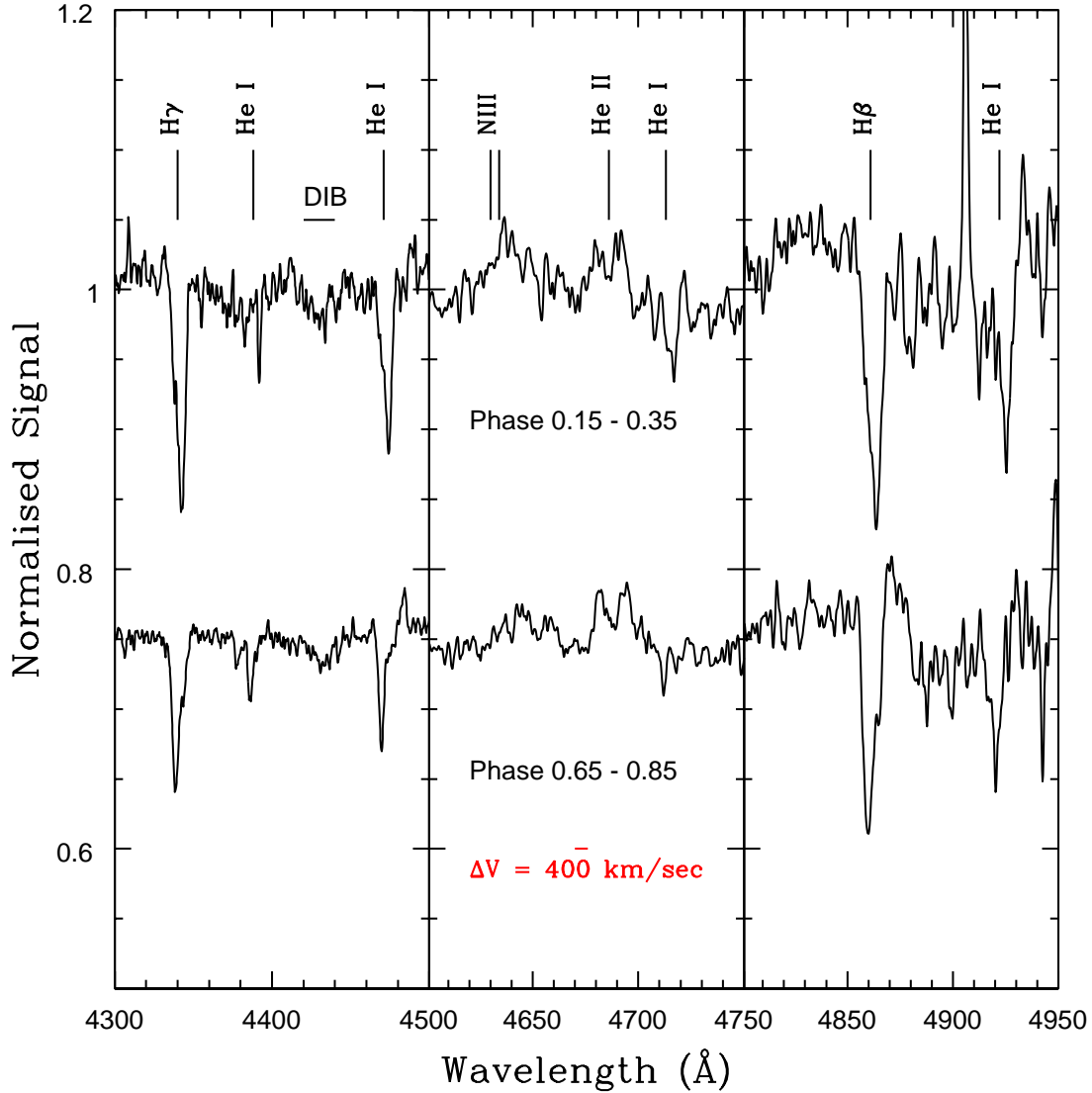


Figure 7. Same as Figure 6, but comparing the 1937 campaign spectra. As in Figure 6 (1) the spectrum of the secondary is clearly evident in many of the absorption lines, (2) the character of N III emission changes with orbital phase, and (3) the emission associated with He II $\lambda 4686$ and in the shoulders of H β tracks the motion of the secondary.

velocities measured from absorption lines may not track faithfully the orbital motions of the component stars. We suggest that the behaviour of the secondary spectrum in the H and He profiles might be affected by an optically thick envelope around that star. If there is transient structuring in the envelope, then this could introduce variations in its velocity measurements with time.

There is evidence of a circumstellar envelope around the secondary. [Wiggs & Gies \(1992\)](#) argue that the wind from the secondary dominates over that from the primary, and the wind will produce a circumstellar envelope. Signatures of an extended envelope around one or both stars are seen in the DAO spectra. The properties of the N III and He II $\lambda 4686$ emission lines are compared in the middle column of Figures 6, 7, and 8. The characteristics of N III emission near 4630\AA in Figures 6 and 7 change with orbital phase, with the lines being widest near phase 0.75. The N III lines are likely photospheric in origin (e.g. [Brucatto & Mihalas 1971](#); [Heap et al. 2006](#)), and phase-related variations are then indicative of asymmetries in the photospheric properties of one or both stars. The relative strengths of the N III lines also change with time with respect to He II $\lambda 4686$ emission, in the sense that these features are weaker near phase 0.25 in the 1922 spectra when compared with the 1937 spectra. Morphological variability in He II $\lambda 4686$

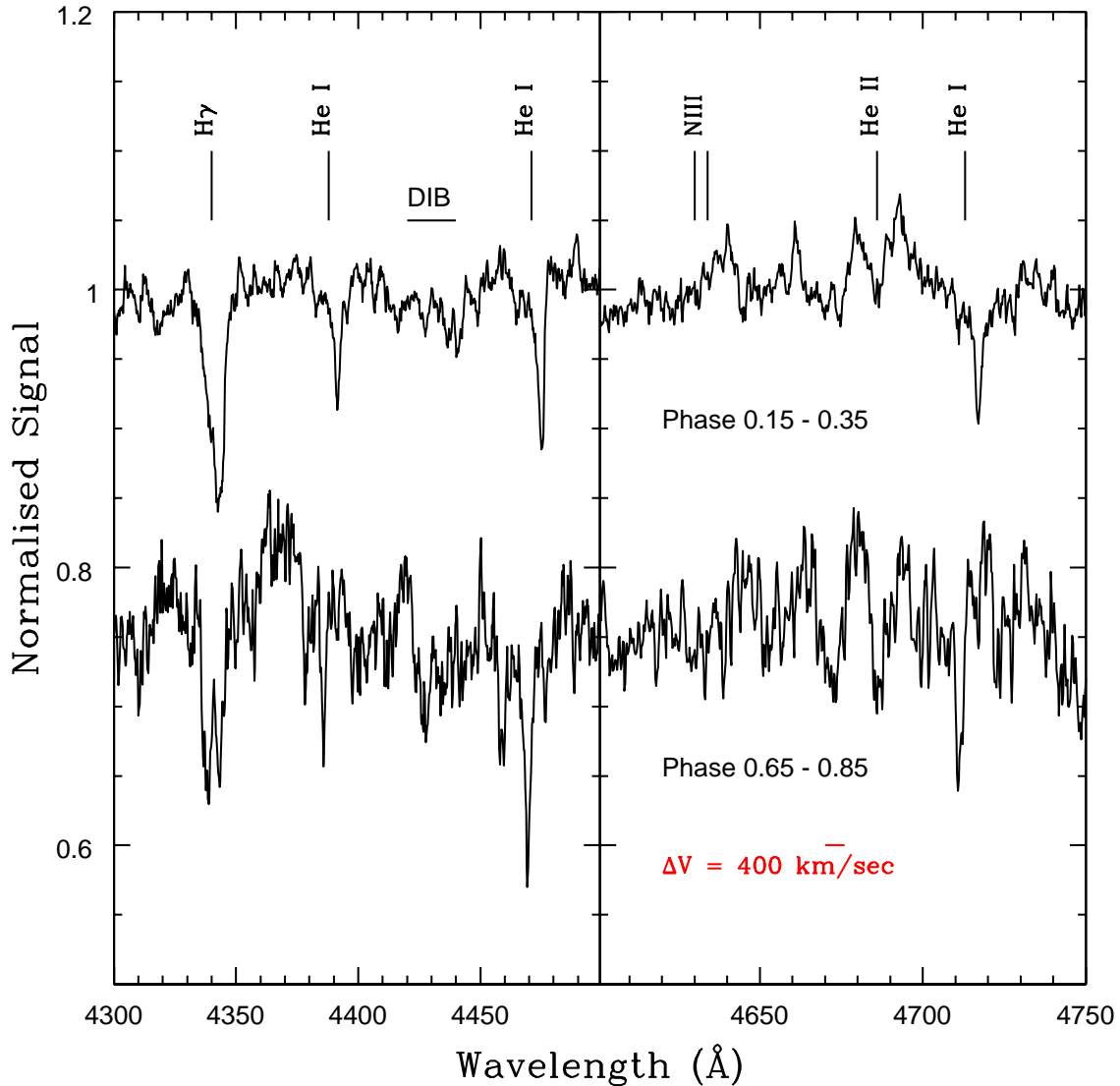


Figure 8. Same as Figure 6, but comparing the 1975 campaign spectra. The wavelength interval covering $H\beta$ is not shown as the S/N is too low to permit a meaningful comparison between orbital phases. The behaviours of the absorption and emission lines are similar to that in Figures 6 and 7.

is seen in O supergiants with spectral types that are similar to the stars in PS, such as HD192639 (Rauw & Vreux 1998).

The emission in the DAO spectra is likely dominated by the secondary and its surroundings. The N III, He II $\lambda 4686$, and $H\beta$ emission in Figure 9 moves in wavelength with orbital phase in the 1922 and 1937 spectra in a manner that is similar to that of the secondary, with the overall change in wavelength being comparable to that found for absorption features associated with that star. A similar shift is not seen in the 1.2 meter 1975 spectra of He II $\lambda 4686$, although the S/N of those spectra is lower than that of the 1.8 meter spectra. There is no evidence for emission associated with the primary. As line emission is associated with the 'f' designation for O stars then these data suggest that an 'f' designation should be assigned to the spectral type of the secondary, but not the primary.

We close this section with a brief discussion of the morphology of He II $\lambda 4686$, and its relation to the properties of the secondary. Venero et al. (2002) model the behaviour of He II lines in a spherically symmetric expanding atmosphere, and link the behaviour of He II $\lambda 4686$ to the properties of the envelope and the host star. For models in which the temperature profile peaks at intermediate radii or climbs steadily with radius, there is an increased tendency

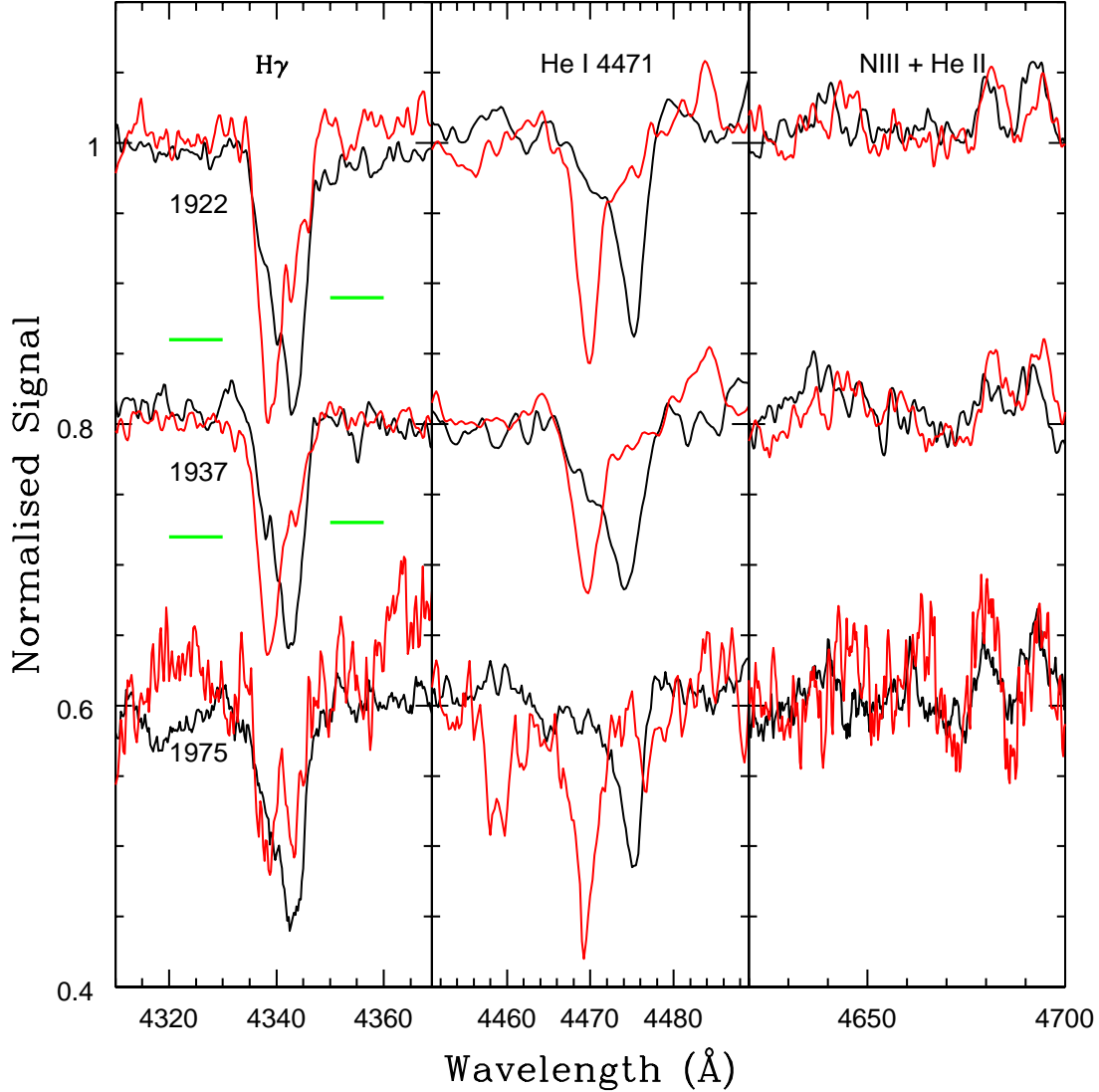


Figure 9. Comparing line profiles near phases 0.25 and 0.75. The black lines are the mean profiles for orbital phases 0.15 - 0.35, while the red lines are for phases 0.65 - 0.85. The spectra for phases 0.65 - 0.85 from 1937 have been scaled by a factor of 1.5 to adjust for the difference in line depths seen in Figure 7. The line profiles do not mirror each other, in the sense that the notch produced by the spectrum of the secondary, which is marked with the green lines near the 1922 and 1937 $H\gamma$ profiles, does not occur at the same depths at the two phases. This is most noticeable in the $H\gamma$ profiles of the 1922 campaign spectra. To the extent that $H\gamma$ tracks the orbital kinematics of the system, then these comparisons indicate that the systemic velocity measured for the secondary from the 1922 campaign spectra differs from that obtained from the 1937 campaign spectra, and this is confirmed with a cross-correlation analysis in Section 6. There is also a tendency for the N III emission lines near 4640Å and for He II $\lambda 4686$ emission/absorption to move with wavelength in a manner that is consistent with the secondary. The presence of N III and He II $\lambda 4686$ emission is consistent with an Of supergiant designation for that star.

for He II $\lambda 4686$ to show the double-peaked morphology seen in the 1.2 meter spectra (1) as $\log(g)$ is lowered, and/or (2) when the emitting region becomes more extended. In the context of these models, a double peaked He II $\lambda 4686$ morphology is consistent with a surface gravity for the secondary that is lower than that of main sequence stars.

The morphology of the He II $\lambda 4686$ profile is also sensitive to the effective temperature of the host star. While the [Venero et al. \(2002\)](#) models do not predict a double peaked profile for an effective temperature of 40000K, such a profile results for effective temperatures of 25000 K. The effective temperature of the secondary in PS is ~ 33000 K

(Linder et al. 2008), and so falls midway between the temperatures modelled by Venero et al. (2002). The general nature of the He II $\lambda 4686$ feature in the PS star is thus broadly consistent with the Venero et al. (2002) models.

Puls et al. (2020) examine model line profiles for hot stars that assume spherical symmetry among the deeper portions of the atmosphere. The models have an approximate resolving power of 10^4 , which is higher than that of the 1.8 meter and 1.2 meter spectra. The double-peaked morphology that is seen in the 1.2 meter spectra, but not the 1.8 meter spectra, is not produced in the models.

The Puls et al. (2020) model that comes closest to matching the effective temperature and $\log(g)$ of the components in PS is s6a, which produces a modest P Cygni-like profile for He II $\lambda 4686$. The absorption and emission components have an amplitude of only a few percent of the continuum level. While this does not match the appearance of the He II profile in the spectra, the character of the profile is temperature-sensitive, and a discernable absorption component disappears in the line profile when the effective temperature is increased to 38700 K. Emission is more prominent in this model, and amounts to $\sim 10\%$ of the continuum level. The emission line for this model is asymmetric in shape, as is seen in some of the 1.8 meter spectra.

5. COMPARISONS WITH SYNTHETIC SPECTRA

Comparisons with synthetic spectra are a means of assessing and validating the information content of the digitized spectra. Agreement between synthetic spectra and the observations would add confidence to our understanding of the observations, and their limitations. This is of particular importance for photographic spectra such as those recorded with the 1.8 meter telescope that are prone to a number of factors that have the potential to compromise their information content (e.g. Section 4.2). We have opted not to compare the 1.2 meter spectra with synthetic spectra given the modest number of high-quality spectra in that sample. Still, the comparisons made in Figure 2 suggests that the conclusions reached here should also apply to those spectra.

Synthetic spectra that cover 4300 – 4551Å were considered. This is near the central wavelength of the observations and contains H γ and He I $\lambda 4471$, which are two of the strongest features in the blue/visible spectrum of late-type O stars. H γ is less susceptible to line emission than H β ; while emission is clearly present in the wings of the latter, it is much more subdued in the former. As the goal of the comparisons is not to use the synthetic spectra to extract or fine tune system parameters, but to assess if the observed spectra – when considered on average – agree with what might be expected from spectra recorded with modern detectors, then a forward modelling approach is adopted.

5.1. Models

The synthetic spectra are based on the solar chemical composition OSTAR2002 models discussed by Lanz & Hubeny (2003) that were generated with TLUSTY (Hubeny 1988; Hubeny & Lanz 1995). The baseline parameters used to construct the synthetic spectra of PS are the effective temperatures (T_{eff}), surface gravities ($\log(g)$), fractional contributions to the light near $0.45\mu\text{m}$ (f_B), observed rotational velocities ($v\sin i$), and the orbital velocity semiamplitudes (K) of both components. The value adopted for each of these to construct the synthetic spectra is shown in Table 3. The entries in this table are taken from Table 3 of Linder et al. (2008), with the $v\sin i$ values being the means of the entries in his table. The quantities in Table 3 generally agree with those found in other studies, and experimentation revealed that tweaking the effective temperatures and surface gravities by small amounts does not greatly alter the synthesized spectra.

The component stars are the only sources of light that are considered in the models. To be sure, there are other sources of light in interacting binary systems, such as emission from disks and outflows. The component stars may also have spots that will alter their spectrophotometric properties. However, as will be demonstrated later in this section, the basic model adopted here reproduces many of the large-scale spectroscopic characteristics of the system.

A spectrum was generated for each component, and the results were smoothed according to their adopted rotational velocities. The synthetic spectra of the components were scaled according to their light contributions, shifted according to the velocity that is appropriate for the orbital phase, and then added together. A model spectrum of the system was constructed for phases near 0.25 and 0.75, as well as near phase 0.0.

5.2. Comparisons with the Observations

Table 3. Parameters Adopted for Synthetic Spectra

Parameter ^a	Star 1	Star 2	Notes
T_{eff}	33500	33000	
$\log(g)$	3.5	3.5	
$vsini$	66	273	(km/sec)
K	202.2	192.4	(km/sec)
f_B	0.65	0.35	

^aAll quantities are from [Linder et al. \(2008\)](#)

The results are compared with the means of spectra within the different phase intervals in Figure 10. The spectra in this figure are the means of all the 1.8 meter spectra within each phase interval that were recorded between 1922 and 1938 that are not of poor quality. Not restricting the means to spectra recorded during the campaigns resulted in a more uniform sampling of phase coverage within each interval.

There is an even mix of spectra from the 1920s and 1930s in the 0.95 – 0.05 and 0.2 – 0.3 phase intervals. Spectrum 7006 was not included when computing the mean spectrum between phases 0.2 and 0.3 because it has shallow absorption lines (e.g. Figure 6). The mean spectrum in the 0.7 – 0.8 phase interval is dominated by 1937 campaign spectra, as only two 1922 campaign spectra fall within this phase interval and were used when taking the mean. Spectrum 7302 has a poor S/N and was not included.

There is mixed success matching the observations. The synthetic spectra overestimate the depth of $H\gamma$ at all three phases, with the agreement between the modelled and observed depth of $H\gamma$ closest between phases 0.95 and 0.05. However, there is approximate agreement between the observed and predicted depths of He I $\lambda 4471$ at all three phases. The synthetic spectra also more-or-less reproduce the skewed line shapes at the orbital quadrature points, although the line widths are not reproduced, in the sense that the model spectra are broader. The differences between the synthetic spectra and observations are in the sense that the amplitude of the orbital velocity of the secondary appears to have been overestimated when constructing the models. The issue of the orbital velocity of the secondary is discussed at greater length in Section 6 and the Appendix.

He I $\lambda 4388$ stands out as it is much deeper than in the synthetic spectra. This line is a singlet transition, and its strength in models is susceptible to uncertainties in the properties of the spectrum near He I $\lambda 584$ ([Najarro et al. 2006](#)). This being said, the inability to reproduce the depth of He I $\lambda 4388$ is not common to all TLUSTY models. [Gonzalez Delgado & Leitherer \(1999\)](#) generate a grid of spectra that use simplified assumptions for opacity and are restricted to predicting the strengths of only H and He lines. The depth of He I $\lambda 4388$ in their models more closely matches that observed in PS. The equivalent widths of $H\gamma$ and He I $\lambda 4471$ predicted by the [Gonzalez Delgado & Leitherer \(1999\)](#) models match very well those in the synthetic spectra generated from the [Lanz & Hubeny \(2003\)](#) models.

In Figure 1 it was shown that there are some differences between the composite 1922 and 1937 campaign spectra, and this leads us to examine if the synthetic spectra match one campaign dataset better than the other. The synthetic spectra are compared with mean spectra from the 1922 and 1937 campaigns in Figure 11. The phase interval 0.7 – 0.8 is not included given that there is only one spectrum in the 1922 campaign (plate 7301) that has a useable S/N.

It was shown earlier that the models did not match the depth of $H\gamma$ in the composite spectra, and this disagreement is greatest in the 1937 campaign spectrum for phases 0.2 – 0.3. The comparisons made in Figure 3 indicate that this is not due to only one spectrum; all three 1937 campaign spectra that were averaged together for this phase interval have similar $H\gamma$ depths. These three spectra were recorded over the course of four consecutive orbital cycles. The synthetic spectra are in reasonable agreement with the width and depth of He I $\lambda 4471$ in most of the spectra in Figure 11. We thus conclude that $H\gamma$ changed strength with orbital phase during the 1937 campaign. Moreover, the depth of $H\gamma$ near phase 0 in the 1937 spectrum is similar to that in the 1922 spectrum at the same phase, and so

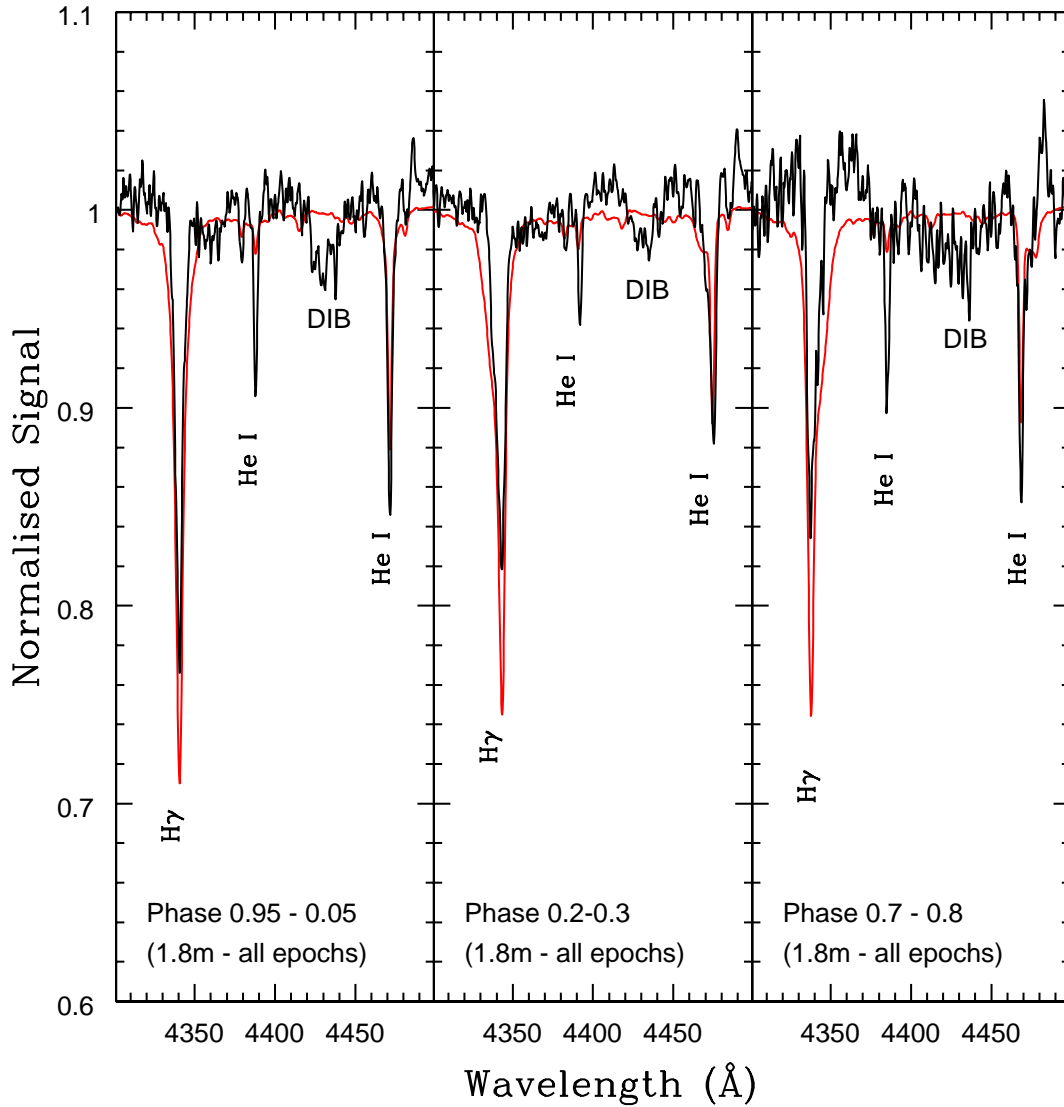


Figure 10. Comparisons with synthetic spectra. The spectra of PS are the means of many of the 1.8 meter spectra recorded between 1922 and 1938 that fall within each phase interval. Spectra 7302 and 7006 were excluded because of poor S/Ns (see text), as were spectra 26304 and 26329 from the 1937 campaign. H γ in the synthetic spectrum is consistently deeper than that observed. There is better agreement with He I λ 4471 at phases 0.2 - 0.3 and 0.7 - 0.8. The models consistently underestimate the depth of He I λ 4388. A comparison of the synthetic and observed line profiles near phases 0.25 and 0.75, including the location of the notch produced by the secondary in the profile, suggests that the overall contribution of the secondary to the total light from the system is more-or-less reproduced in the synthetic spectrum. However, that the synthetic spectra are broader than the upper portions of H γ and He I λ 4471 near phases 0.25 and 0.75 is consistent with the orbital velocity of the secondary having been overestimated.

it is likely that the comparatively shallow nature of H γ between phases 0.2 and 0.3 during the 1937 campaign was a transient phenomenon that was not present during the 1922 campaign.

If the depths of features in the PS spectra are taken at face value then a better match to the depth of H γ may be found if the effective temperature of the primary in the models were to be increased and/or if the surface gravity were changed at some phases. This could occur if the temperature distribution across the face of the primary was not uniform, perhaps due to a spot or a reflection effect from a hot area associated with the secondary and/or its surroundings. The TLUSTY-based model H and He line strengths discussed by [Gonzalez Delgado & Leitherer \(1999\)](#)

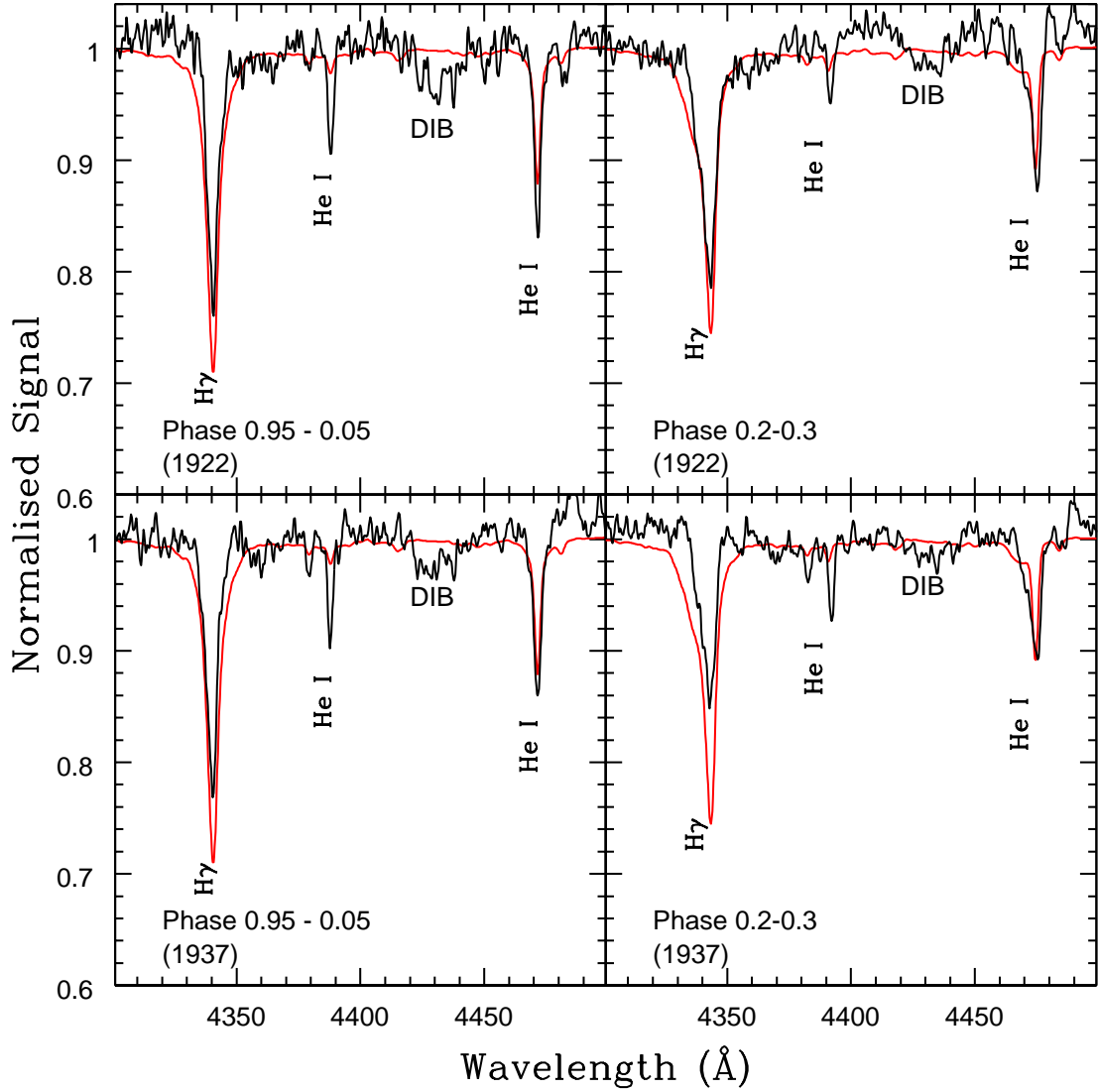


Figure 11. Comparing campaign and synthetic spectra. The spectra of PS are the means of the 1.8 meter spectra from the 1922 (top panel) and 1937 campaigns (bottom row). The phase interval 0.7 – 0.8 is not included because there is only one useable spectrum that samples this interval in the 1922 dataset. $H\gamma$ is consistently larger in the synthetic spectra than in either group of campaign spectra, with the difference being greatest for the 1937 spectra between phases 0.2 and 0.3. In contrast, the depth of He I $\lambda 4471$ is more-or-less reproduced by the models. It is argued in the text that the comparatively shallow nature of $H\gamma$ near phase 0.25 in the 1937 spectrum was a transient phenomenon.

provide a convenient means of assessing the dependence of H and He line strengths on parameters such as effective temperature and surface gravity.

The [Gonzalez Delgado & Leitherer \(1999\)](#) models suggest that if the side of the primary that faced the observer at phase 0.25 during the 1937 campaign had an effective temperature that was $\sim 5000\text{K}$ hotter than the rest of the star then this could largely explain the relative depths of $H\gamma$ and He I $\lambda 4471$. However, models with a main sequence surface gravity are then required for the primary if its spectrum is to match the observed $H\gamma/\text{He I } \lambda 4471$ ratio, and this is contrary to the luminosity class assigned to this star by most studies. Moreover, the ratio of He II $\lambda 4541$ to He I $\lambda 4471$ is a gauge of effective temperature, and this line ratio among spectra near phase 0.25 in the 1937 campaign spectrum agrees well with that measured from the 1922 campaign spectrum – the relative depths of these lines are thus consistent with the effective temperature not changing with time.

The comparisons with the models thus lead us to suspect that the relatively shallow depth of $H\gamma$ in the 1937 campaign spectra near phase 0.25 cannot be due to surface temperature variations. While not explored here, perhaps the variations in the depth of $H\gamma$ may be due to abundance spots, such as those seen in Ap and Bp stars. In any event, the possibility that the depth of $H\gamma$ is affected by the response of the photographic plate seems unlikely. This is because the spectra recorded in 1937 near this phase over different nights have similar $H\gamma$ depths. A similarity in bogus line depths would then be due to either a statistical fluke or a systematic issue in the plates that were used for the observations near phase 0.25, but not at other phases, which is highly improbable.

6. CROSS-CORRELATION FUNCTIONS AND THE MASS RATIO

Lines with different excitation conditions at blue wavelengths in the PS spectrum yield similar velocities (Bagnuolo & Barry 1996), and so the information content in the PS spectra can be multiplexed by using a cross-correlation procedure to measure velocities. In addition to radial velocities, CCFs also contain information about the overall strengths of features in the spectra of the components. The CCFs discussed here were generated with the FXCOR task in IRAF, which is based on a program described by Tonry & Davis (1979).

The CCFs discussed in this section were generated in the 4300 – 4600Å wavelength interval, which samples the peak optical response of the 1.8 meter spectra. The largest single contributors to the CCFs are then $H\gamma$ and He I $\lambda 4471$, although weaker features also contribute to the CCFs. Extending the coverage to longer wavelengths to include $H\beta$ produces slightly noisier CCFs, although the location of the peaks associated with the components do not change markedly. Velocities obtained from the 1.8 meter spectra using the 4300 – 4600Å range and those that use the full wavelength coverage of the spectra are compared in the Appendix.

The reference spectrum used to obtain the CCFs is a combination of H, He, and N lines with depths that are taken from the median 1922 campaign spectrum in Figure 1. To the extent that the spectrum of the secondary is suppressed when spectra that are aligned on the centers of strong lines in the primary are combined, then the template is a proxy for the spectrum of the primary. Absorption lines in the template are δ functions that extend down from a flat continuum, and the template is compared with 1922 campaign spectra near orbital phases 0.25 and 0.75 in Figure 12. The use of an unbroadened spectrum as a reference template more cleanly separates the peaks in the CCF that form from lines in the spectra of the two components, which can blend together if real stellar spectra are used as a reference, such as in Figures 5 and 6 of Bagnuolo et al. (1999). The use of an unbroadened template for velocity measurements was first suggested by Furenlid & Furenlid (1990).

Emphasis is placed on orbital phases 0.25 and 0.75, where the velocity difference between the stars is greatest, thereby yielding the half amplitudes of the stellar motions (K_1 and K_2). There are multiple spectra between phases 0.2 and 0.3 in the 1922 and 1937 campaign datasets. However, while there are five spectra between phases 0.7 and 0.8 in the 1937 campaign dataset, there is only one spectrum (7301) from the 1922 campaign in this phase interval that is suitable for velocity measurements; spectrum 7302 has a very poor S/N, and produces a problematic CCF.

Two spectra from the 1.2 meter observations are also considered: 8820 at phase 0.2, and 9545 at phase 0.73. While the former is not part of the 1975 campaign, it is the only useable 1.2 meter spectrum that samples a phase close to 0.25. The 1.2 meter spectra are of interest when interpreting the CCFs as they were recorded with an image slicer, and so are less susceptible to variations in spectral resolution due to seeing variations. The 1.2 meter spectra are intrinsically noisier than the 1.8 meter spectra, and so they were smoothed with a 0.25Å Gaussian to enhance the S/N before generating the CCFs.

CCFs that sample orbital phases near 0.25 and 0.75 are shown in Figures 13 (1.8 meter) and 14 (1.2 meter). Distinct peaks that are associated with the primary and secondary are clearly visible in Figure 13. While not as well defined as in Figure 13, features that can be identified with the secondary are also apparent in Figure 14.

The CCFs differ in appearance from those obtained by Stickland (1997), in the sense that the difference in heights between the peaks associated with the primary and secondary are much larger than found by Stickland (1997). This difference is perhaps not surprising as the Stickland CCFs were constructed from UV spectra. The difference in peak heights reflects the relative light contributions from the two stars, which are more closely matched in the UV than near 4400Å.

The separation between the peaks that correspond to the primary and secondary in Figures 13 and 14 are smaller than found by Stickland (1997), amounting to 100 – 190 km/sec as opposed to 300 km/sec from the Stickland CCFs of SWP 4819 and SWP 13924 in his Figure 4. In the Appendix it is argued that this is likely due in large part to the wavelength resolution of the DAO spectra. Still, the difference in velocity between the two components obtained

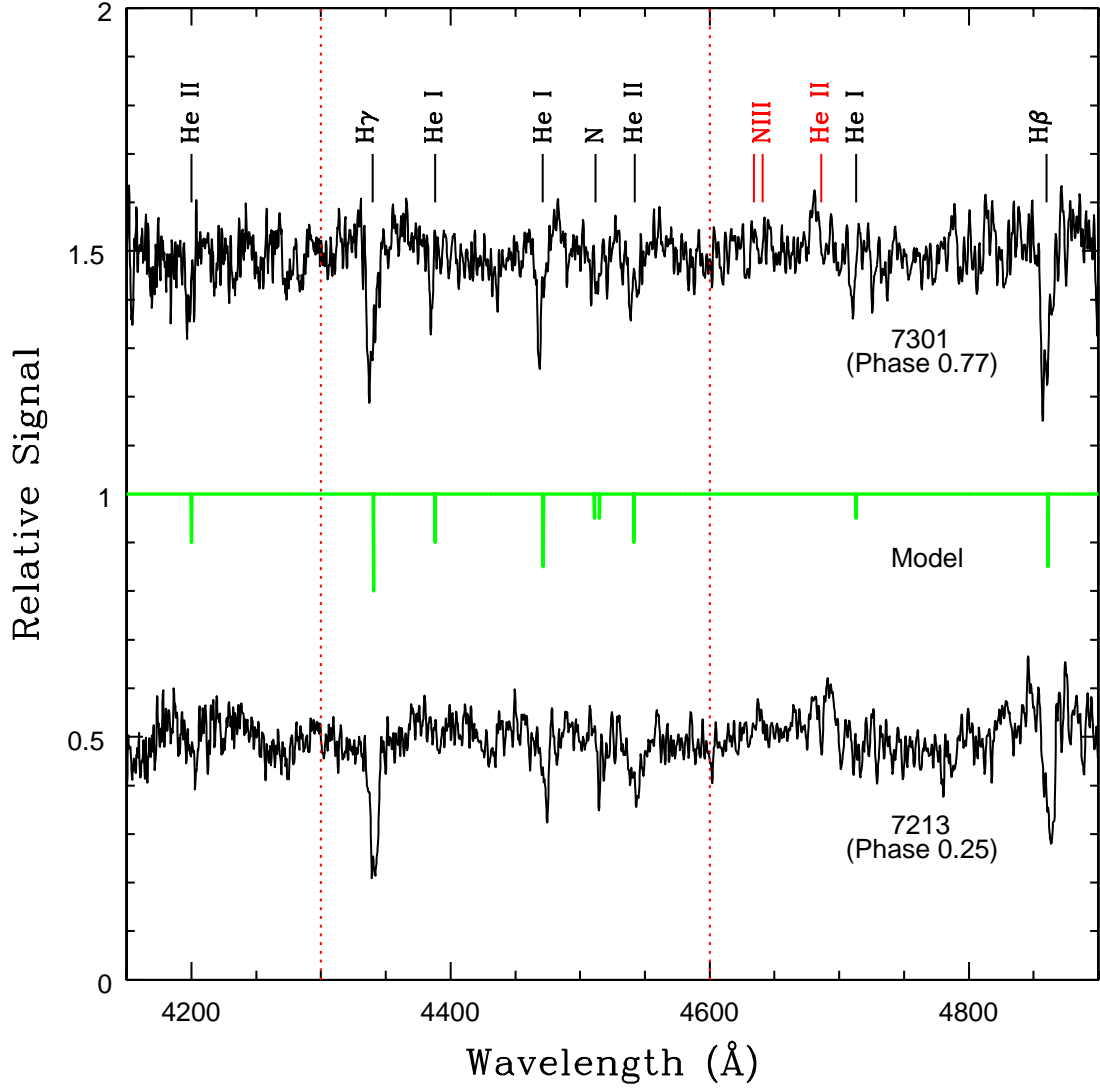


Figure 12. Spectra from the 1922 campaign that sample orbital phases near 0.25 and 0.75 are compared with the CCF template, shown in green. The template consists of unbroadened lines that correspond to H, He, and N transitions, with depths based on those of the actual lines in the median 1922 campaign spectrum. The dotted lines mark the boundaries of the wavelength interval used to generate the CCFs.

from spectrum SWP 4819 in Figure 4 of [Stickland \(1997\)](#) is smaller than that in spectrum SWP 13924. This, along with other factors, lead Stickland to conclude that the velocities of the secondary 'make no sense dynamically'.

The peak associated with the secondary near phase 0.75 in Figure 13 changes location with time, in the sense that the offset between the signatures of the primary and secondary in the CCF of spectrum 7301 from the 1922 campaign is larger than that in spectrum A22101 from the 1937 campaign. It should be recalled that line shapes in the 1922 and 1937 campaign spectra at phase 0.25 differ because of the location of the notch associated with the secondary in each profile (Section 4). The difference in line profiles is consistent with the behaviour of the secondary feature in Figure 13.

While establishing a velocity amplitude for the secondary is complicated by the variations in the location of the peak attributed to that star, it is clear that the amplitude of the orbital velocity variations of the secondary is smaller than that of the primary. The smaller amplitude of the radial velocity curve of the secondary is consistent with it being more massive than the primary. If mass transfer has occurred then PS is a post-Algol binary.

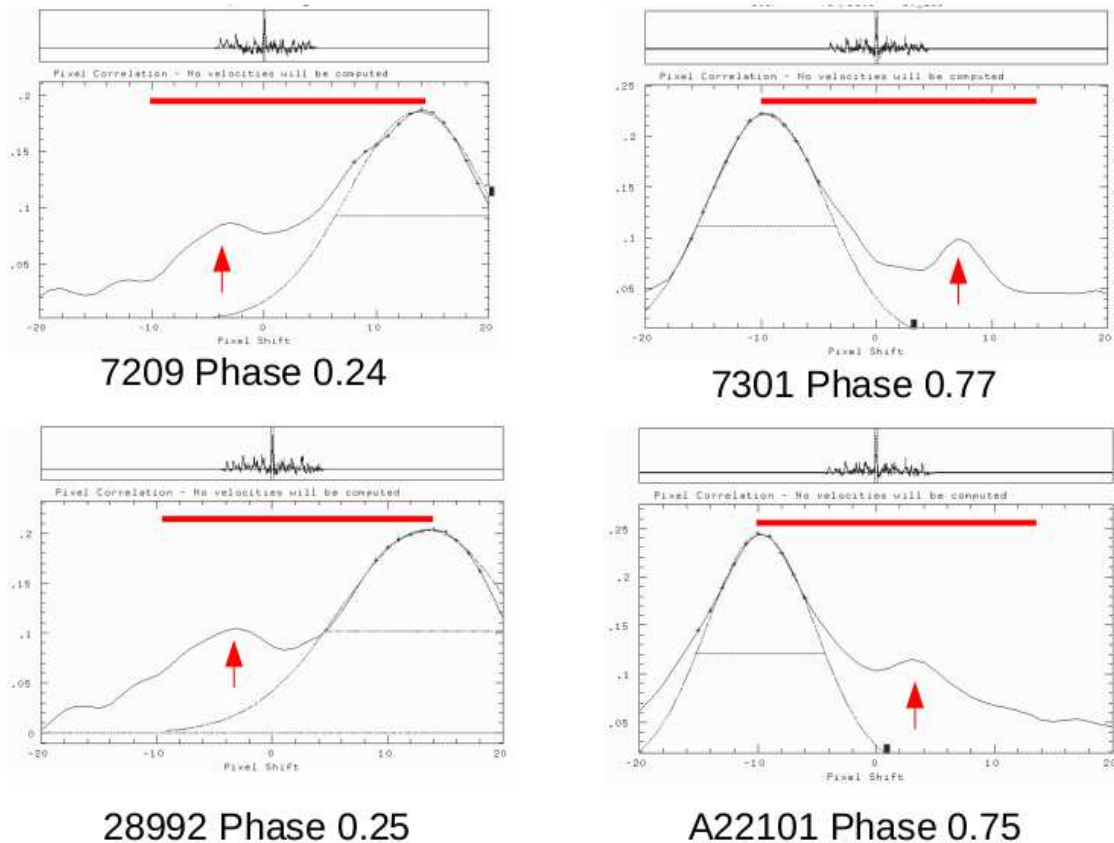


Figure 13. CCFs of 1.8 meter spectra near orbital phases 0.25 and 0.75 from the 1922 (top row) and 1937 (bottom row) campaigns. The spectra have been cross-correlated with the reference spectrum between wavelengths 4300 and 4600Å using the IRAF task FXCOR. The dominant peak in the CCFs is formed by lines in the spectrum of the primary, while a lower amplitude peak due to the secondary is marked with a red arrow. The thick red line has a length of 400 km/sec, which is the approximate full amplitude of the radial velocity variation of the primary. The separation between the peaks due to the primary and secondary varies, corresponding to $\sim 100 - 190$ km/sec, which is smaller than the difference in component velocities found in most other studies. That the radial velocity amplitude of the secondary is smaller than that of the primary is consistent with it being the more massive star. The dashed line is a Gaussian fit to the peak from the primary. The width of the peak in the CCFs formed by the primary near phase 0.25 is greater than that near phase 0.75, and this is also seen in the CCFs of the 1.2 meter spectra in Figure 14.

Based on the velocity measurements discussed in the Appendix, we estimate a velocity half amplitude of 90 km/sec for the secondary, and a ratio of amplitudes of 0.5 ± 0.1 , in the sense primary over secondary. The mass ratio is then 2.0 ± 0.4 . This is substantially larger than most previous estimates, and yields lower component masses than found in previous studies. Adopting the [Stickland \(1997\)](#) mass function, then with a mass ratio of $2 M_1 \sin(i)^3 = 14.2 \pm 1.2$ and $M_2 \sin(i)^3 = 28.3 \pm 2.7 M_\odot$.

The orbital inclination is uncertain as the system is not eclipsing. [Bagnuolo et al. \(1992\)](#) argue for a value between 69.3 and 72.7 degrees based on the radius of the components, while [Rudy & Herman \(1978\)](#) estimates an inclination of 71 ± 9 degrees from polarimetry. Adopting $i = 71^\circ$ yields masses of 17 and 34 M_\odot , while if $i = 62^\circ$ based on the lower limit from [Rudy & Herman \(1978\)](#) then the masses are 21 and 42 M_\odot .

Given the substantial uncertainties in the properties of the secondary and the difficulties extracting its spectroscopic signatures from these moderate dispersion spectra then the mass ratio and mass estimates should be viewed with caution. Arguably the most robust conclusion that can be drawn from the CCFs in Figures 13 and 14 is that the secondary is more massive than the primary. Determining an improved mass ratio will require a better understanding of what is causing the velocity measurements that are attributed to the secondary to drift with time.

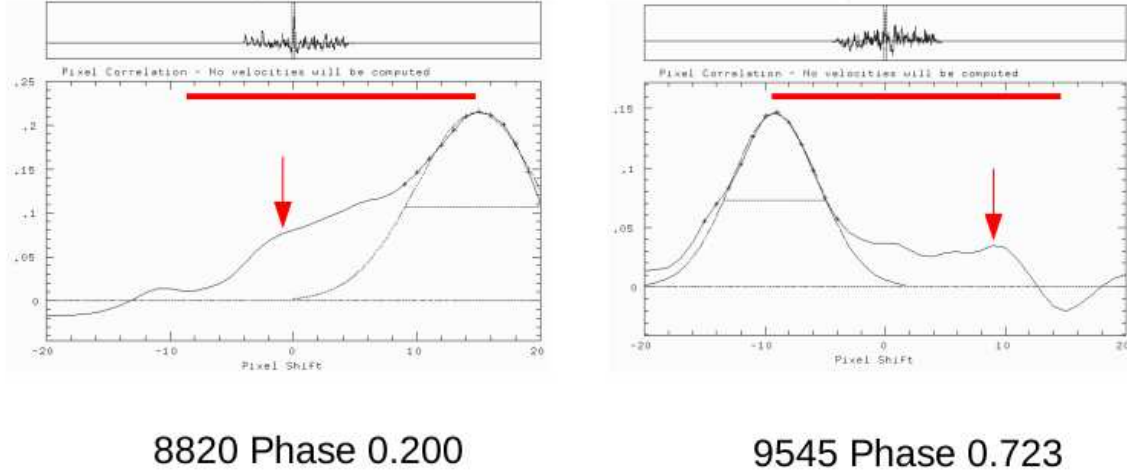


Figure 14. Same as Figure 13, but showing CCFs constructed from 1.2 meter spectra. The peak due to the secondary is less well-defined than in Figure 13, reflecting the lower S/N of the 1.2 meter spectra. Still, the velocity amplitude based on these CCFs is consistent with that obtained from the 1922 campaign spectra. As in Figure 13, the peaks are broader near phase 0.25 than near phase 0.75. As the 1.2 meter spectra were recorded with an image slicer then it is unlikely that this broadening is a consequence of seeing variations.

In Section 4.3 it was suggested that the system line profiles might be explained if there is a component in the spectrum that is related to the secondary but that also has velocities that do not track faithfully the orbital motion of that star. If the wind from the secondary is the dominant contributor to material being fed into the intracomponent medium (Wiggs & Gies 1992), then we suggest that the velocities obtained from the absorption spectrum that is associated with the secondary may be skewed by transient optically thick material in the outflow from that star. Even small-scale perturbations in the winds of evolved O stars are expected to induce clumping (e.g. Hawcroft et al. 2021, and references therein), and we suggest that it is the transient motion of such clumps that might affect the radial velocity measurements that are attributed to the secondary.

7. DISCUSSION & SUMMARY

We have discussed photographic spectra of PS that were recorded with the 1.2 and 1.8 meter telescopes at the DAO. The spectra sample the wavelength region $0.39 - 0.49\mu\text{m}$ (1.8 meter) and $0.35 - 0.55\mu\text{m}$ (1.2 meter) with wavelength resolutions of a few thousand. The spectra were digitized with a flat-bed scanner, and the results were processed according to the procedures described by Davidge (2024).

The spectra were recorded over a 5 decade time span from the early 1920s to the mid 1970s, and provide insights into the evolution of PS during much of the past century, prior to the widespread use of digital detectors. Many of the 1.8 meter spectra were obtained during campaigns in the 1922 and 1937 observing seasons, and so provide snapshots of the PS system at those times. The 1922 campaign spectra were the basis of the discovery paper by Plaskett (1922), and are among the oldest extant spectra of this system. To the best of our knowledge, the spectra recorded in the 1930s have not been discussed in the published literature.

The S/N of the data used here is admittedly low, and can easily be surpassed with even short duration exposures with modern detectors. Still, spectra of this nature are the only means available to study the properties of stars prior to circa 1980. As of late 2024, the PS system has undergone over 2600 orbital cycles since the first 1.8 meter spectrum was recorded. The DAO spectra thus provide an anchor for examining the long term evolution of the PS system.

A complication when examining spectra of this vintage is that they do not form a homogeneous dataset. The quality of the digitized DAO spectra range from very poor to very good, and this is due in part to environmental factors, such as cloud cover, seeing variations, etc. There are also spectra where there is evidence of issues with the instrumentation, such as the mis-alignment of optical components, as well as with the handling and development of the photographic plates. Plates that will likely be problematic for future studies have been identified.

7.1. Line Strengths and Velocity Variations

Information has been extracted from the digitized spectra that is supplemental to that found in earlier studies where the plates were examined in their undigitized form. Comparisons of spectra recorded within a campaign and between campaigns have been made. While the response characteristics of photographic materials is certainly a limiting factor, the overall agreement between spectra within a campaign and between campaigns after they have been combined to suppress the effect of environmental factors on the observations suggests that *on average* the spectra have similar response characteristics in the intensity range covered by the spectra.

Variations in the strengths of some lines, most notably $H\gamma$, have been found, and evidence has been presented that these are intrinsic to the system spectrum. Variations in the strengths of lines in the spectrum of an SB2 that contain early-type stars are not rare, and a subset of these variations have been termed the Struve-Sahade (S-S) effect. Line strength variations due to the S-S effect are typically attributed to the spectrum of the secondary, in the sense that the lines are weaker when the star is receding and stronger when it is approaching. The physical cause of the S-S effect remains a matter of discussion (e.g. Linder et al. 2007; Palate et al. 2013). However, it is not clear if a classic S-S effect has been detected in the PS spectrum (e.g. Stickland 1997; Bagnuolo et al. 1999; Linder et al. 2008). The variations we see in the strength of $H\gamma$ are associated with the primary.

Prominent line emission is seen in the digitized spectra, as expected given the 'f' designation that has been assigned to the system spectral type. Linder et al. (2008) suggest that He II $\lambda 4686$ and $H\alpha$ emission forms in a wind around the secondary star that is flattened along the orbital plane. In fact, the wavelength motion of He II $\lambda 4686$ in the digitized spectra is consistent with it being associated with the secondary. This holds also for N III emission and emission seen in the shoulders of $H\beta$. This is consistent with the secondary having the dominant wind. The association of the N III emission with the secondary suggests that its spectral type should be assigned an 'f' designation.

The digitized spectra have been compared with synthetic spectra that are based on system properties summarized by Linder et al. (2008). Groups of spectra that were averaged to suppress environmental and instrumental effects are in broad agreement with the synthetic spectra, even though no effort has been made to tune the system parameters to achieve an optimum match with the observations. The secondary produces features in the observations that have counterparts in the synthetic spectra, and the locations of these signatures in the system line profiles are consistent with previous estimates of the light contribution made by the secondary to the total system light output.

Noticeable departures from the synthetic spectra are seen for $H\gamma$ at some epochs as well as He I $\lambda 4388$. The latter is an indicator of luminosity class (e.g. Martins 2018), although the disagreement between the predicted and observed depths of this feature may be due to deficiencies in the extent of line blanketing near 584\AA in the models (Najarro et al. 2006). The variations in the depth of $H\gamma$, if intrinsic to the primary, can not be explained by varying the effective temperature of that star in a manner that is consistent with its other properties.

While it is difficult to judge the strengths of individual features from the secondary in many of the individual DAO spectra, CCFs provide a blunt means of judging the composite strength of features in the spectra of the components. The relative amplitude of the peak attributed to the secondary in the CCFs shown in Figures 13 and 14 does not appear to vary when compared with that of the primary, suggesting that the relative strengths of lines in the spectra of the components near the quadrature points remain constant. This is indirect evidence against a S-S effect in the spectrum of PS.

The morphologies of the CCFs near phases 0.25 and 0.75 obtained from the DAO spectra differ from those constructed from UV spectra (e.g. Stickland 1997), in the sense that the peak attributed to the secondary in Figures 13 and 14 has a smaller amplitude with respect to that of the primary than is seen in CCFs constructed from UV spectra. This is largely due to the difference in wavelengths, as the relative contributions made by the components to the total system light at a given wavelength depends on factors such as the effective temperature and the properties of circumstellar and intrasystem material. The template used to construct the CCF from the DAO spectra also differs from that employed by Stickland (1997), who used the spectrum of the O8 star HD99486.

A more traditional use for CCFs is to measure the motions of stars. Evidence was presented in Section 6 that the velocities measured from the peak in the CCFs that is attributed to the secondary varies with time in a manner that suggests they may not faithfully track its orbital motion, as noted previously by Stickland (1997). This is clearly seen in the DAO spectra, where the peak in the CCF that is attributed to the secondary at phase 0.75 changes position with time.

Velocity measurements for all DAO 1.8 meter spectra near the orbital quadrature points are presented in the Appendix, and these indicate that the amplitude of the secondary velocity curve did not change between 1922 and 1937. The amplitude of the velocity curve of the secondary measured from CCFs is much smaller than that of the

primary, and is consistent with a mass ratio ~ 2 . This is markedly larger than most previous estimates (but see also Grunhut et al. (2022)).

Previous studies have found inherent uncertainties in the spectrum of the secondary that will complicate attempts to find a mass ratio. For example, there is considerable scatter in the velocities measured for the secondary by Linder et al. (2008), and they attribute this to factors such as line intensity variations. These uncertainties can have a sizeable influence on the estimated mass ratio. Inspection of Figure 2 of Linder et al. (2008) demonstrates that the orbital velocities of the secondary near phases 0.25 and 0.75 are not well-defined. A velocity curve that were to pass through the mean of the points near these phases in Linder et al. (2008) Figure 2, as opposed to the peak values, would have a half-amplitude that is lower than that adopted by Linder et al. by ~ 40 km/sec. This would change the mass ratio obtained from the Linder et al. spectra from 1.05 to 1.3, placing the mass ratio in better agreement with that obtained from UV spectra by Bagnuolo et al. (1992). More recently, Grunhut et al. (2022) present evidence that the secondary rotates with a period of 1.2 days, and find no evidence of orbital motion in its Stokes V profiles. This argues for a lower amplitude radial velocity variation for the secondary than has previously been seen, further bringing into question the orbital properties of the secondary found in past studies.

One possible explanation for the kinematic characteristics of the secondary is that the absorption lines attributed to that star may reflect transient activity in its circumstellar environment. Modest variations in the behaviour of He II $\lambda 4686$ (e.g. Figure 9) lend some support to this argument. Variations in He II lines are seen in the spectra of other evolved O stars, and these have been attributed to large-scale inhomogeneities (e.g. Rauw & Vreux 1998) or rotational modulation in the wind (e.g. Rauw et al. 2001).

The width of the peak in the CCF that is formed by the primary changes with orbital phase, and this is seen in observations that span a range of epochs and instrumentation. Perhaps most significantly, this phase-dependent broadening is evident in CCFs constructed from 1.2 meter spectra, which were recorded through an image slicer, rather than a slit. The variation in the width of the CCF is then not due to the way in which the entrance to the spectrograph was illuminated, as might occur due to seeing variations if a slit were in place, but is intrinsic to the spectrum.

The change in the width of the primary peak in the CCF suggests that the spectroscopic properties of that star are not symmetric in the orbital plane, and previous evidence for this is seen in the behaviour of $H\gamma$ in the 1937 campaign spectra. There are only modest variations in the system light output with orbital phase, and so any physical mechanism that drives changes in the line profiles of the primary, that in turn sets the width of the primary peak in the CCF, can not induce large changes in the visible brightness of that star. If the asymmetric spectroscopic properties of the primary in the orbital plane that are hinted at from the width of the CCF are due to (say) mass accretion onto the primary, then the modest variations in the light curve indicates that there is not a spot on the surface of the primary or a surrounding disk with an effective temperature that differs greatly from its surroundings.

7.2. The Evolutionary Status of PS: Past and Future

It is widely accepted that PS experienced mass transfer after the primary evolved into contact with its critical Roche surface. Evidence to support this is the rapid rotation of the secondary due to the accretion of angular momentum from the primary, and the CNO surface abundances of the stars (e.g. Bagnuolo & Barry 1996; Linder et al. 2006, 2008) that are indicative of core processed material that has been brought to the surface, as might be expected if the primary had evolved off of the main sequence prior to mass transfer. The evidence that the fainter secondary is now more massive than the brighter primary at visible wavelengths is a further indication that there has been mass transfer.

Stacey et al. (2024) suggest that PS may be a highly evolved system, in which the primary has lost most of its mass and is now a heavily stripped, bloated remnant. Evidence for this comes from the radial velocity variations deduced from the Stokes V profile measurements made by Grunhut et al. (2022). If $K_2 = 30$ km/sec as found by Grunhut et al. (2022) then the system mass ratio is $\frac{202}{30} = 6.7$. The component masses are then $M_1 \sin i^3 = 2.5 M_\odot$ and $M_2 \sin i^3 = 16.7 M_\odot$. Adopting $i = 71^\circ$ as was done in Section 6 then the component masses would be roughly 3 and $20M_\odot$; the latter is close to that expected for an O8 main sequence star.

Based on more recent observations than those examined by Grunhut et al. (2022), Stacey et al. (2024) find that the radial velocity amplitude of the secondary may be even smaller than that reported by Grunhut et al. (2022). If this is the case then the masses of the primary and secondary would be pushed to even lower values than those stated in the previous paragraph. Still, the mass function obtained by Stickland (1987) indicates that the lower mass limit for the secondary is $12.6 \sin i^3 m_\odot$.

The lack of large-scale structure in the system light curve with a cadence that matches the orbital period indicates that the components of PS are not at present in contact with their Roche surfaces. This is consistent with PS being a post-Algol system. That the primary in early-type systems can detach from its Roche surface after mass transfer is predicted by models. Peng et al. (2022) model a $30 + 27M_{\odot}$ system with a 20 day initial period. Following mass transfer, the mass losing star eventually de-couples from its Roche surface and is able to regain thermal equilibrium.

The future evolution of PS is difficult to predict given the inherent uncertainties in our understanding of the early evolution of stars in massive binary systems (e.g. Belczynski et al. 2022). Still, the component separation may decrease in the immediate future. Mass that is lost from PS due to winds will remove angular momentum from the system, thereby shortening the period. Moreover, if the secondary is more massive than the primary and has the dominant wind (e.g. Wiggs & Gies 1992) then there will likely be a net transfer of mass from the secondary to the primary, and this will also decrease the component separation.

One of the stars in PS will eventually evolve into contact with its critical Roche surface and induce another episode of large-scale mass transfer. This will affect the separation of the components, although it is not obvious if the next lobe-filling star will be the primary or the secondary. While the secondary is now more massive than the primary, it is also rotating at a much faster rate, and so mixing will extend its evolutionary timescale when compared with that expected for a non-rotating star. If there is another mass transfer event that is spurred by the evolution of the primary then this should cause the separation of the components to increase, although this depends on the rate of mass loss from the system if the mass transfer is not conservative.

7.3. Future Work

There is considerable scope for future work, and a recommended emphasis is on observations that will help to better understand the nature of the secondary. There is uncertainty in the amplitude of the velocity curve of the secondary, and thus the system masses. Spectra that examine PS through a number of sequential cycles would be of interest to chart variations in the velocity curve of the secondary, and place limits on the timescale of any variations in the amplitude of its orbital velocity curve. That the radial velocity amplitudes of the secondary obtained from the 1922 and 1937 campaign spectra appear to differ indicates that the amplitude can change on timescales ≤ 15 years, although other velocity measurements for the secondary (e.g. Linder et al. 2008) suggest a shorter timescale. An investigation of this nature could also explore possible correlations with lines that are associated with stellar winds, such as He II $\lambda 4486$ and lines in the UV that show P Cygni profiles. These spectra might also provide information that could be used to assess if clumping is a possible cause of the velocity variations.

The behaviour of $H\gamma$ in the spectrum of the primary near phase 0.25 could also be examined with spectra that span a number of orbits, with an emphasis on determining if variations in line strength and velocity (see the Appendix) are seen with modern detectors. As the cyclicity of these variations are not known, then this could require monitoring over a longer term. If variations in the strength of $H\gamma$ are found then it would be of interest to search for signs of possible abundance variations at this same phase, as abundance spots may be one cause of these variations.

It is a pleasure to thank the anonymous referee for providing a comprehensive report that greatly improved the manuscript.

APPENDIX

A. RADIAL VELOCITIES

These data were originally recorded to measure radial velocities as part of a survey of early-type stars. In this section, we discuss velocity measurements extracted from the digitized spectra using different techniques, with a goal of assessing the velocity information that can be extracted, especially with regards to the secondary. The spectra recorded in the 1920s are of particular interest, as they can be compared with the original measurements that were made by Plaskett (1922).

Many of the 1.2 meter spectra tend to be of poor quality, and so the discussion is restricted to 1.8 meter spectra. In addition, as the moderate wavelength resolution of the 1.8 meter spectra complicates efforts to isolate features from the secondary, then only spectra that sample the phase intervals 0.15 – 0.35 and 0.65 – 0.85 are considered. These are the points in the orbit where the velocity difference between the primary and the secondary is largest, thereby enhancing the chances of de-coupling the spectroscopic signatures of the stars.

Table 4. Radial Velocities Measured Between 4100Å to 4600Å

Plate #	HJD	Phase	V ₁ (km/sec)	V ₂ (km/sec)
6953	23053.838	0.297	182.0	-37.2
7006	23067.849	0.27	188.0	-68.5
7138	23104.753	0.834	-142.7	137.3
7193	23109.733	0.18	191.9	-101.2
7209	23110.632	0.242	202.2	-54.0
7213	23110.736	0.249	221.6	-60.8
7217	23111.675	0.315	218.0	-54.0
7282	23124.689	0.219	220.4	-54.0
7301	23132.635	0.771	-191.9	112.0
7302	23132.808	0.783	-166.9	138.5
7304	23133.633	0.84	-129.9	80.8
26236	28459.062	0.758	-219.4	64.0
26367	28494.051	0.188	182.0	-37.2
26568	28552.854	0.272	235.6	-74.2
26649	28595.736	0.251	244.1	-54.0
26726	28630.661	0.677	-100.9	182.0
28624	29178.027	0.699	-210.6	102.2
28992	29257.906	0.247	150.6	-116.7
A22101	29322.704	0.748	-151.4	64.0

In Figure 13 it is demonstrated that the spectrum of the secondary forms a prominent feature in the CCF, and so cross-correlation provides a compelling means of extracting velocity information for the secondary. Velocities were measured with the IRAF FXCOR task, using the wavelength interval between 4100 and 4600Å. This interval is where the S/N is highest, and is also where there is a concentration of prominent absorption lines, of which H γ and He I λ 4471 are the strongest. The model template described in Section 6 was used as the reference for the cross-correlation, and experimentation found that the velocities are not sensitive to the presence of the DIB near 4400Å. Moreover, they did change markedly when the wavelength range was expanded. The results are presented in Table 4, while the velocities are shown as a function of orbital phase in the upper panel of Figure A1. The estimated uncertainties in individual velocity measurements vary with data quality, but are typically 5 – 15 km/sec.

We estimate the amplitude of the velocity curve at each epoch by taking the mean velocity of the primary and secondary in each phase interval and then taking the difference. The full amplitude of the primary velocity curve is 361 ± 15 km/sec in the 1920s, and 373 ± 36 km/sec in the 1930s. These tend to be lower than the full amplitudes found from more recent studies because they are averages over a large range of the system orbit. The full amplitude of the secondary velocity curve from the 1920s measurements is then 179 ± 16 km/sec while the narrow measurements from the 1930s gives an amplitude 174 ± 31 km/sec. The uncertainties are $1 - \sigma$ formal errors of the mean. The ratio of the amplitudes is then 0.48 ± 0.11 .

The cores of individual deep lines provide robust velocity estimates for the brighter star that are less susceptible to contamination from a fainter companion. Velocities were measured from the cores of H γ and He I λ 4471, which are among the most prominent features in the 1.8 meter spectra, and the results are tabulated in Table 5, where the means of the H γ and He I λ 4471 measurements are in the final column. The estimated uncertainties are ± 10 km/sec.

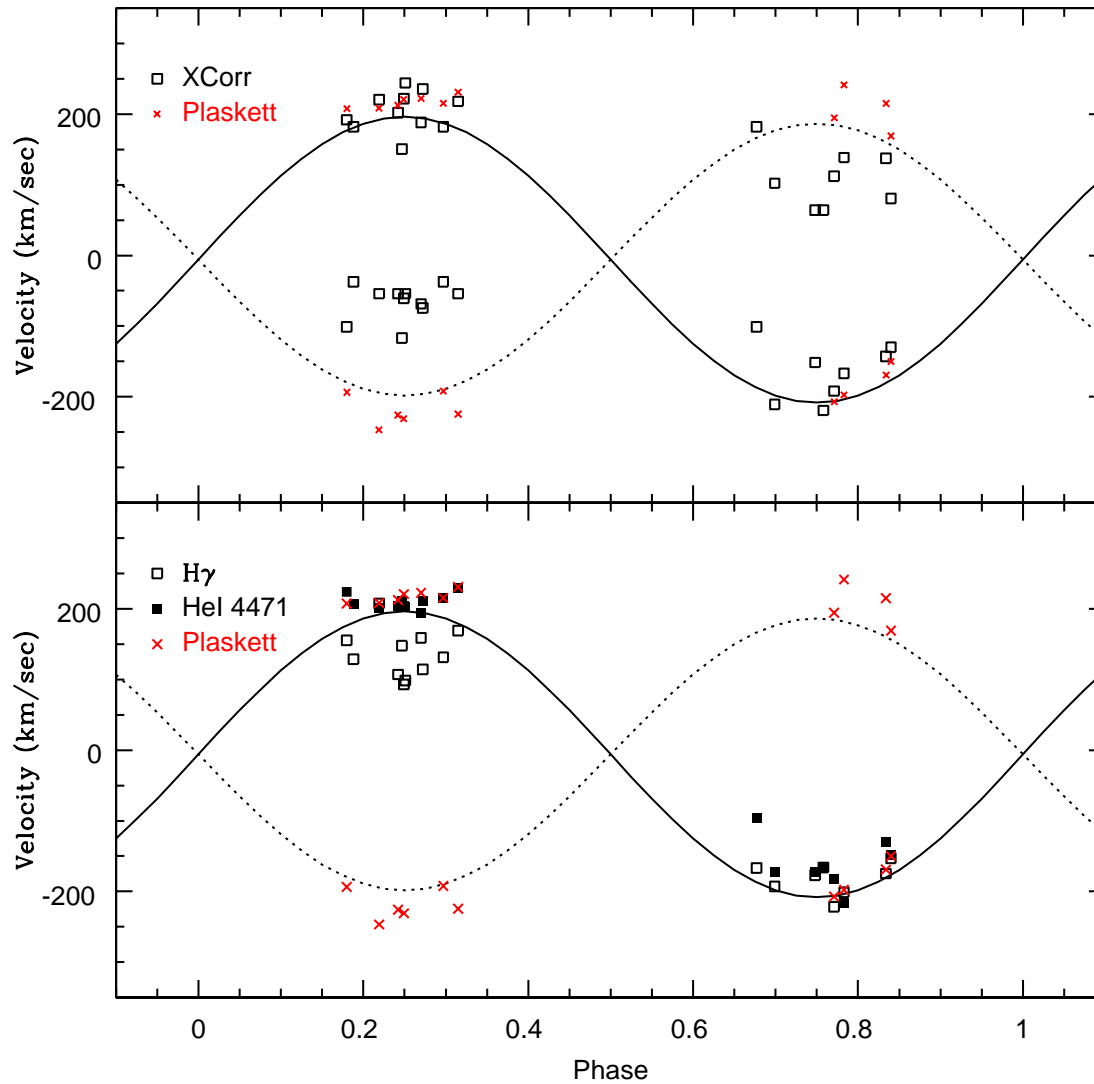


Figure A1. Radial velocities measured from digitized 1.8 meter spectra using different techniques. The top panel shows CCF-based velocities while the lower panel shows velocities of the primary estimated from the cores of $H\gamma$ and He I $\lambda 4471$. The red crosses in both panels are the velocities measured by Plaskett (1922) from a number of lines and summarized in his 'Table of Velocities and Residuals'. The solid and dashed curves are the radial velocity curves based on the orbital elements calculated by Linder et al. (2008).

We have not attempted to extract velocities for the secondary from line centroids given the heavily blended nature of the lines. The $H\gamma$ and He I $\lambda 4471$ velocities are plotted in the lower panel of Figure A1.

The He I velocities near phase 0.25 have modest scatter when compared with their $H\gamma$ counterparts. Moreover, the amplitude of the velocity curve defined by He I $\lambda 4471$ is also comparable to that found in previous studies, although there might be a slight offset in the system velocity obtained from this line. What is most noticeable is that while $H\gamma$ is the most prominent feature in these spectra and is arguably the best defined, it shows a marked departure from the Linder et al. (2008) velocity curve near phase 0.25. At this phase the $H\gamma$ velocities are consistently lower than those obtained from He I $\lambda 4471$. This offset holds for measurements made from both the 1920s and 1930s spectra. The strength of $H\gamma$ at this phase also differs from that at other phases (e.g. Section 4.2). The agreement between the

Table 5. Radial Velocities Measured From Cores of H γ and He I λ 4471

Plate #	HJD	Phase	V_H (km/sec)	V_{He} (km/sec)	V_{Mean} (km/sec)
6953	23053.838	0.297	131.4	214.8	173.1
7006	23067.849	0.27	158.9	194.27	176.6
7138	23104.753	0.834	-174.7	-129.9	-152.3
7193	23109.733	0.18	155.6	224.1	189.9
7209	23110.632	0.242	107.0	203.8	155.4
7213	23110.736	0.249	93.2	203.8	148.5
7217	23111.675	0.315	168.9	230.3	199.6
7282	23124.689	0.219	207.7	200.8	204.3
7301	23132.635	0.771	-221.8	-182.6	-202.2
7302	23132.808	0.783	-201.1	-216.2	-208.6
7304	23133.633	0.84	-152.8	-149.2	-151.0
26236	28459.062	0.758	-166.0	-167.0	-166.5
26367	28494.051	0.188	128.8	206.1	167.4
26568	28552.854	0.272	114.3	211.2	162.7
26649	28595.736	0.251	98.6	202.3	150.4
26726	28630.661	0.677	-166.59	-95.4	-131.0
28624	29178.027	0.699	-192.6	-172.7	-182.7
28992	29257.906	0.247	147.8	210.6	179.2
A22101	29322.704	0.748	-177.1	-172.6	-174.8

H γ and He I velocities is better near phase 0.75. We note that [Plaskett \(1922\)](#) stated that H γ tended to give 'good velocity measures', although even some of these were 'somewhat discrepant'.

In summary, the comparisons made in this section indicate that velocities made from the core of He I λ 4471 in the digitized spectra match those originally obtained by [Plaskett \(1922\)](#), and track velocity variations that are based on the orbital elements found by [Linder et al. \(2008\)](#). The velocity measurements for the primary star made directly from the plates by [Plaskett \(1922\)](#) thus appear to be consistent in quality with those obtained from He I λ 4471 in the digitized spectra. As for measurements made from CCFs, we find that the full amplitude of the velocity curve of the secondary is substantially smaller than found by [Plaskett \(1922\)](#). This argues for a mass ratio that is substantially different from near unity.

REFERENCES

- Bagnuolo, W. G., Gies, D. R., & Wiggs, M. S. 1992, *ApJ*, 385, 708
- Bagnuolo, W. G., & Barry, D. J. 1996, *ApJ*, 469, 347
- Bagnuolo, W. G., Gies, D. R., Riddle, R., & Penny, L. R. 1999, *ApJ*, 527, 353
- Belczynski, K., Romagnolo, A., Olejak, A., et al. 2022, *ApJ*, 925, 69
- Bik, A., Henning, Th., Wu, S.-W., et al. 2019, *A&A*, 624, A23
- Bonatto, C., & Bica, E. 2009, *MNRAS*, 394, 2127
- Brucatto, R. J., & Mihalas, D. 1971, *MNRAS*, 154, 491
- Davidge, T. J. 2022, *RNAAS*, 6, 175
- Davidge, T. J. 2024, *AJ*, 167, 249
- Draper, H. 1877, *Nature*, 15, 218
- Furenlid, I., & Furenlid, L. 1990, *PASP*, 102, 592
- Gaia Collaboration, Prusti, T., de Bruijne, J. H. J. et al. 2016, *A&A*, 595, A1
- Gaia Collaboration, Brown, A. G. A., Vallenari, A., Prusti, T. et al. 2022, *A&A*, 649, A1
- Gonzalez Delgado, R. M., & Leitherer, C. 1999, *ApJS*, 125, 479
- Grunhut, J. H., Wade, G. A., Folsom, C. P., et al. 2022, *MNRAS*, 512, 1944
- Hawcroft, C.m Sana, H., Mahy, L., et al. 2021, *A&A*, 655, A67
- Heap, S. R., Lanz, T., & Hubeny, I. 2006, *ApJ*, 638, 409
- Herbig, G. H. 1975, *ApJ*, 196, 129
- Hubeny, I. 1988, *Compt. Phys. Commun.*, 52, 103
- Hubeny, I., & Lanz, T. 1995, *ApJ*, 439, 875
- Hutchings, J. B., & Cowley, A. P. 1976, *ApJ*, 206, 490
- Lanz, T. & Hubeny, I. 2003, *ApJS*, 146, 417
- Linder, N., Rauw, G., Pollock, A. M. T., & Stevens, I. R. 2006, *MNRAS*, 370, 1623
- Linder, N., Rauw, G., Sana, H., De Becker, M., & Gosset, E. 2007, *A&A*, 474, 193
- Linder, N., Rauw, G., Martins, F., et al. 2008, *A&A*, 489, 713
- Mahy, L., Gosset, E., Baudin, F., et al. 2011, *A&A*, 525, A101
- Martins, F. 2018, *A&A*, 616, A35
- Mees, C. E. K. 1931, *JOSA*, 21, 753
- Mees, C. E. K. 1933, *JOSA*, 23, 299
- Mees, C. E. K. 1935, *JOSA*, 25, 80
- Najarro, F., Hillier, D. J., Puls, J., Lanz, T., & Martins, F. (2006), *A&A*, 456, 659
- Oke, J. B. 1969, *PASP*, 81, 110
- Palate, M., Rauw, G., Koenigsberger, G., & Moreno, E. 2013, *A&A*, 552, A39
- Palate, M., & Rauw, G. 2014, *A&A*, 572, A16
- Peng, W., Song, H., Meynet, G., et al. 2022, *A&A*, 657, A116
- Plaskett, J. S. 1918, *PDAO*, 1, 1
- Plaskett, J. S. 1921, *PDAO*, 1, 325
- Plaskett, J. S. 1922, *MNRAS*, 82, 447
- Puls, J., Najarro, F., Sundqvist, J. O., & Sen, K. 2020, *A&A*, 642, A172
- Rauw, G., & Vreux, J.-M. 1998, *A&A*, 335, 995
- Rauw, G., Morrison, N. D., Vreux, J.-M., Gosset, E., & Mulliss, C. L. 2001, *A&A*, 366, 585
- Richardson, E. H. 1968, *JRASC*, 62, 313
- Robinson, L. B., & Wampler, E. J. 1972, *PASP*, 84, 161
- Rudy, R. J., & Herman, L. C. 1978, *PASP*, 90, 163
- Sen, K., Langer, N., Marchant, P., et al. 2022, *A&A*, 659, A98
- Simcoe, R. J. 2009, *ASPC*, 410, 111
- Stacey, E., Wade, G. A., Grunhut, J. H., Folsom, C. P., & Kochukhov, O. 2024, *IAUS* 361, 366
- Stickland, D. J. 1987, *The Observatory*, 107, 68
- Stickland, D. J. 1997, *The Observatory*, 117, 37
- Struve, O. 1948, *ApJ*, 107, 327
- Struve, O., Sahade, J., & Huang, S-S 1958, *ApJ*, 127, 148
- Tody, D. 1986, *SPIEE*, 627, 733
- Tody, D. 1993, *ASPC*, 52, 173
- Tonry, J., & Davis, M. 1979, *AJ*, 84, 1511
- Venero, R. O. J., Cidale, L. S., & Ringuet, A. E. 2002, *ApJ*, 578, 450
- Wiggs, M. S., & Gies, D. R. 1992, *ApJ*, 396, 238